bioRxiv preprint doi: https://doi.org/10.1101/2024.11.07.622471; this version posted November 8, 2024. The copyright holder for this preprint (which was not certified by peer review) is the author/funder. All rights reserved. No reuse allowed without permission.

Follicular Bcl6 reactivity is associated with a unique immune landscape and spatial transcriptome in COVID-19

Cloe Brenna[1], Bramon Mora Bernat[2], Kalliopi Ioannidou[1], Simon Burgermeister[1], Julien Bodelet[3], Mia Siebmanns[1], Spiros Georgakis[1], Michail Orfanakis[1], Nazanin Sédille[4], Matthew J Feinstein[5], Jon W Lomasney[5], Oliver Y. Chen[3], Giuseppe Pantaleo[6], Sabina Berezowska[1], Laurence De Leval[1], Raphael Gottardo[2], Constantinos Petrovas[1]

[1]Institute of Pathology, Department of Laboratory Medicine and Pathology, Lausanne University Hospital and Lausanne University, Lausanne, VD, Switzerland.

[2]Biomedical Data Science Center, Lausanne University Hospital and Lausanne University, Lausanne, VD, Switzerland.

[3]Department of Laboratory Medicine and Pathology, Lausanne University Hospital and Faculty of Biology and Medicine, University of Lausanne, Lausanne, Switzerland.

[4]Service of Clinical Chemistry, Department of Laboratory Medicine and Pathology, Lausanne University Hospital and Lausanne University, Lausanne, VD, Switzerland.

[5]Feinberg School of Medicine of Northwestern University, Chicago, IL, USA.

[6] Service of Immunology and Allergy, Department of Medicine, Lausanne University Hospital and Lausanne University, Lausanne, VD, Switzerland.

Corresponding author

Constantinos Petrovas, PhD, Department of Laboratory Medicine and Pathology, Institute of Pathology, Lausanne University Hospital, Rue du Bugnon 25, CH - 1011 -Lausanne, Switzerland, Konstantinos.Petrovas@chuv.ch

Keywords: COVID-19, follicles, immune landscaping, spatial transcriptomics, multiplex imaging

Short title: Lymph node immune landscaping in COVID-19

Conflicts of Interest

R.G. has received consulting income from Takeda, Sanofi, and declares ownership in Ozette Technologies and Modulus Therapeutics.

bioRxiv preprint doi: https://doi.org/10.1101/2024.11.07.622471; this version posted November 8, 2024. The copyright holder for this preprint (which was not certified by peer review) is the author/funder. All rights reserved. No reuse allowed without permission.

ABSTRACT

The regulation of follicular (F) and germinal center (GC) immune reactivity in human lymph nodes (LNs), particularly during the early stages of viral infections, remains poorly understood. We have analyzed lung-draining lymph nodes (LD-LNs) from COVID-19 autopsies using multiplex imaging and spatial transcriptomics to examine the immune landscape and with respect to the aging. We identified three subgroups of Reactive Follicles (RFs) based on Bcl6 prevalence, RF-Bcl6no/low, RF-Bcl6int and RF-Bcl6high. RF-Bcl6high tissues express a distinct B/TFH immune landscape associated with increased prevalence of proliferating B- and TFH-cell subsets. Comparison between LD-LNs and matched subdiaphragmatic LNs revealed a disconnected Bcl6 reactivity between the two anatomical sites. LD-LNs Bcl6 reactivity was associated with a distinct spatial transcriptomic profile. TH1-associated genes/pathways (e.g. CXCR3, STAT5, TNF signaling) were significantly upregulated in RF-Bcl6no/low tissues while the RF-Bcl6high tissues exhibited significant upregulation of GC-promoting genes/pathways (e.g. CXCL13, B cell receptor signaling). Despite the similar prevalence, the in-situ transcriptome profiling indicates a higher monocyte/macrophage functionality in “Aged” compared to “Young” follicles from donors with comparable Bcl6 reactivity. Our findings reveal a heterogeneous F/GC landscape in COVID-19 LD-LNs and highlight specific molecular targets and pathways that could regulate human F/GC immune dynamics during early viral infections.

bioRxiv preprint doi: https://doi.org/10.1101/2024.11.07.622471; this version posted November 8, 2024. The copyright holder for this preprint (which was not certified by peer review) is the author/funder. All rights reserved. No reuse allowed without permission.

INTRODUCTION

The COVID-19 pandemic, caused by SARS-COV-2, has significantly impacted global health, highlighting the urgent need to understand the human immune responses against the virus(1). Particularly vulnerable groups, such as the elderly and individuals with comorbidities, are at higher risk for severe effects and mortality(2). Age-related immune decline, or "immunosenescence", further compromises the ability to effectively combat infections and respond to vaccination(3).

Lymph Nodes (LNs) are crucial for shaping immune responses against pathogens(4). With respect to respiratory infections, thoracic LNs, e.g. Hilar Lymph Nodes (HLNs), located in the lung hilum, are of particular interest as they host antigen-presenting cells (APCs) that capture viral antigens from the lungs, facilitating the activation of naïve T-cells into effectors to fight the virus. Within the germinal centers (GCs), the coordinated function of TFH-cells and GC B-cells can lead to the development of pathogen-specific B-cell responses(5). TFH cells assist B cells in undergoing somatic hypermutation (SHM) and affinity maturation, essential for producing high-affinity antibodies and long-term immune memory. Acute COVID-19 infection has been associated with a reduction in GCs and compromised expression of $Bcl6^{high}$ cells, alongside an overexpression of TNF-α that could impair the TFH-cell differentiation and development of GC immune reactivity leading to the generation of long-term B-cell memory(6). This impairment may lead to a compromised response upon reinfection or exposure to new variants(7). The study of relevant lung-draining lymph nodes (LD-LNs) could also provide insights into regional immune responses like effector CD8 T-cells in the lungs, the primary site of SARS-COV-2 infection.

The cellular and molecular mechanisms underlying the development of human GC immune reactivity, particularly in early viral infections, are not well understood. Lack of access to relevant tissues represents a major challenge for such research. Although COVID-19 infection is associated with a highly inflammatory environment in moderate and severe diseases not necessarily found in other viral infections(8), using relevant COVID-19 autopsies could provide useful information regarding basic immunological mechanisms mediating the development of GC reactivity.

The primary aim of our study was to deepen our understanding of GC immune reactivity in the context of COVID-19. To achieve this, we examined LD-LNs from both "Aged" (≥60 years) and "Young" (<57 years) individuals, employing serological measurements, multiplex

bioRxiv preprint doi: https://doi.org/10.1101/2024.11.07.622471; this version posted November 8, 2024. The copyright holder for this preprint (which was not certified by peer review) is the author/funder. All rights reserved. No reuse allowed without permission.

immunofluorescence imaging (mIF), and spatial *in situ* transcriptomic profiling. This approach allowed us to characterize the cellular and molecular landscape within these LNs during SARS-CoV-2 infection, with a particular focus on how Bcl6 expression relates to the formation of distinct RF profiling. Our findings highlight age-related differences in RFs, with Bcl6 expression corresponding to unique cellular profiles and molecular signatures within the germinal center. Mechanistically, our data suggest that in COVID-19 infection, overexpression of a TH1 follicular signature may hinder the formation of mature RFs, particularly in LD-LNs.

bioRxiv preprint doi: https://doi.org/10.1101/2024.11.07.622471; this version posted November 8, 2024. The copyright holder for this preprint (which was not certified by peer review) is the author/funder. All rights reserved. No reuse allowed without permission.

MATERIALS AND METHODS

Human material.

LN tissues were obtained from the Institute of Pathology at Lausanne University Hospital, Switzerland, and the Feinberg School of Medicine of Northwestern University **(Tables 1 and 2)**. Postmortem examinations and autopsies from patients who died of COVID-19 disease were performed **i)** at the Institute of Pathology of Lausanne University Hospital (CHUV) between March 2020 and March 2021 and **ii)** Department of Pathology, Northwestern University between March 2020, and July 2021. The studies were approved by the Ethical Committee of **i)** the Canton de Vaud, Switzerland (protocol number 2020-01257) and **ii)** Northwestern University (STU# 00202918). Written consent was obtained from all living participants, and in cases where samples were previously donated to tissue repositories from deceased patients, an IRB-approved waiver of consent was applied (Northwestern University, CHUV). Tonsillar tissues were obtained from anonymized children who underwent routine tonsillectomy at the Hospital de l'Enfance of Lausanne, with approval from the Canton de Vaud-CER-VD, Switzerland (PB_2016-02436 (201/11)). This research project was conducted according to the principles of the Declaration of Helsinki.

Sex as a biological variable. Our study examining both male and female participants. Due to the small sample size, sex was not considered as a covariate in this investigation. Our cohort comprised 20 males (14 in the "Aged" group and 6 in the "Young" group) and 12 females (10 in the "Aged" group and 2 in the "Young" group).

Plasma was collected from some of the participants using EDTA as an anticoagulant. An immunoturbidimetric assay was employed for the quantification of CRP levels. Absolute numbers of leukocytes (G/L), lymphocytes (G/L), neutrophils (G/L), monocytes (G/L), eosinophils (G/L), and basophils (G/L) were determined using an automated hematology analyzer.

Multiplex Immunofluorescent (mIF)-data acquisition.

4µm thick sections were prepared from formalin-fixed, paraffin-embedded (FFPE) blocks and mounted on Superfrost glass slides (Thermo Scientific, Waltham). The sections were then used for mIF and spatial transcriptomic (GeoMx) analysis. The tissue staining involved several sequential steps as previously described(9). Antigen retrieval was followed by blocking of non-

bioRxiv preprint doi: https://doi.org/10.1101/2024.11.07.622471; this version posted November 8, 2024. The copyright holder for this preprint (which was not certified by peer review) is the author/funder. All rights reserved. No reuse allowed without permission.

specific antibody binding using the Opal blocking/antibody diluent solution. Then, titrated primary antibodies and appropriate secondary HRP-labeled antibodies were applied **(Tables 3 and 4)**. The detection of the target proteins was achieved using optimized fluorescent Opal tyramide signal amplification (TSA) dyes (Akoya), along with repeated cycles of antibody denaturation. To visualize the cell nuclei, the sections were counterstained with Spectral DAPI. Following staining, the sections were rinsed in water with soap and mounted using DAKO mounting medium from Dako/Agilent, Santa Clara. Multispectral images (MSI) were acquired using **i)** the Vectra Polaris 1.0 imaging system (Akoya) at a resolution of 5µm/pixel (20x) and **ii)** a Leica Stellaris 8 SP8 confocal system, equipped with LAS-X software (at 512 × 512-pixel density and 20× objective). A compensation matrix, which was created using the Leica LAS-AF Channel Dye Separation module (Leica Microsystems) and tissue sections stained with a single antibody–fluorophore, was used to correct fluorophore spillover across different channels.

Imaging data analysis.

For the Vectra Polaris-generated images, the Phenochart 1.0.12 software (Akoya), a whole-slide viewer for high-resolution multispectral acquisition and annotation capabilities, was used to navigate among slides and identify specific Regions of Interest (ROIs). The subsequent imaging and analysis were performed on the whole tissue. The acquired MSI were analyzed using the InForm analysis software, version 2.4.8 (Akoya). Initially, the images were unmixed, and specific ROIs were used for the algorithm training and cell segmentation across the imaged tissue. The segmentation process involved utilizing the appropriate training components, such as CD20, BCL6, and PD1 to define the GC, Extrafollicular area (EF), and region without tissue. Tissue segmentation was based on selected training markers and DAPI expression, extracting the autofluorescence signal of the tissue. This was achieved by manually drawing training regions for each analyzed image. The segmentation algorithm was trained individually on each image, ensuring a training accuracy of over 90% for the ROIs segmentation. Next, individual cells were segmented using an adaptive cell segmentation algorithm based on the counterstained sections. Cytoplasm and membrane markers were utilized to help in this cell segmentation process. A file report was generated, containing the spatial coordinates (X, Y) of each segmented cell, along with their mean intensity for each Opal fluorophore used. This file report was then extracted and converted into a FACS file (FSC) format before being uploaded to the FlowJo 10 software and the generated data were further analyzed with

bioRxiv preprint doi: https://doi.org/10.1101/2024.11.07.622471; this version posted November 8, 2024. The copyright holder for this preprint (which was not certified by peer review) is the author/funder. All rights reserved. No reuse allowed without permission.

HistoFlowCytometry(10). Data are reported as normalized numbers per µm2 or frequency of total imaged cells.

Morphological characteristics of follicular areas

Morphological analysis of individual follicular ROIs, identified based on the density of $CD20^{high/dim}$ B cells, was carried out using FIJI software, where various features such as the area, circularity, and solidity were extracted. To ensure robust analysis, approximately 20 ROIs per tissue were meticulously chosen, each representing distinct and well-defined follicular structures within the tissues. Subsequently, from each ROI, the follicle areas were extracted and normalized using the tissue scale bar. This normalization process ensured that the follicle areas were accurately represented relative to the tissue dimensions, facilitating meaningful comparisons across samples.

Distance Analysis and Spatial Distribution

To investigate the spatial relationship between relevant cell types (GC-B and TFH-cell subsets), the minimum distance between individual B-cells and TFH-cells, within follicles expressing more than 20 positive cells for each population, was calculated with Python 3.10.9 using the Scipy library(11). The matrix interaction was generated using X and Y coordinates from each cell type and the median distance was extracted. The probability of observing different patterns of cellular distribution across individual ROIs and patients was investigated by analyzing the curves generated from the Ripley's G function and the theoretical Poisson curve using Pointpats 2.3.0(12). The area between the empirical and theoretical Poisson curve was extracted using the NumPy library(13). The data were presented either as bar graphs (range of all various distances measured x-axis vs frequency or count of B-cells within each distance range y-axis) or dot plots, with each dot representing the mean value of the minimum Euclidean distances between two cell populations for each follicular area (ROI).

Tissue Spatial Transcriptomic analysis

Transcriptomic profiling was performed using the commercially available platform GeoMx Digital Spatial Profiling (Nanostring). 4 µm FFPE tissue sections from n= 8 RF-Bcl6no/low "Aged" and n=7 RF-Bcl6no/low "Young", n=3 RF-Bcl6int "Aged" and n=3 RF-Bcl6int "Young", and n=3 RF-Bcl6high "Aged", were used. Follicular Regions of Interest (ROIs, n=9-12 per slide) were identified based on the corresponding mIF image and the CD3, CD20 *in situ* staining pattern before the probe-hybridization step. ROIs were selected within a range of areas,

bioRxiv preprint doi: https://doi.org/10.1101/2024.11.07.622471; this version posted November 8, 2024. The copyright holder for this preprint (which was not certified by peer review) is the author/funder. All rights reserved. No reuse allowed without permission.

and quantitative analysis revealed an average area of 245,745.52μm^2 (± 211,116.16 μm², SD). The data were collected in two different experiments (A and B). The DSP GeoMx software was used for the PCA analysis of specific gene sets among the section ROIs.

Data Processing and Quality Control: We analyzed NanoString DSP data using standard GeoMx processing workflows(14), and R version 4.3.2. Specifically, we processed the DCC files and conducted quality control at the segment, probe, and gene levels using the R packages "GeoMxWorkflows"(14), "GeomxTools"(15), and "NanoStringNCTools"(16). First, we adjusted all zero expression counts to one to enable subsequent data transformations. We then implemented several quality control metrics recommended by NanoString for our segments, including a minimum of 1000 reads, 80% trimming, stitching, and alignment, 50% sequencing saturation, a minimum negative control count of 1, a maximum of 1000 reads observed in NTC wells, and a minimum area of 1000. Next, we removed probes for which the average count across segments was less than 10% of the average count for all probes targeting the same gene across segments, as well as probes that were outliers in at least 20% of the segments. Finally, we filtered out segments and genes with low signal, specifically removing segments where less than 5% of panel genes were detected above the level of quantification (LOQ, defined as two standard deviations above the mean) and genes detected below the LOQ in at least 10% of segments.

Batch Correction: to perform batch correction, we first normalized the raw data using the Trimmed Mean of M-values (TMM) method with the R package "standR"(17), which adjusts for differences in library sizes and composition between RNA-seq samples. We then applied the RUV-4 correction from the same package(18), which removes unwanted variations by identifying negative control genes and calculating scaling factors for batch correction. In our analysis, we identified 300 negative control genes and set the number of scaling factors to 2.

Differential Gene Expression and Enrichment Analysis: to perform differential gene expression, we followed the limma-voom pipeline(19). We defined a linear model with a design matrix containing the treatment variable and weight matrix from the RUV-4 correction method as covariates. Using this model, we then compared every pair of treatments, identifying differentially expressed genes as those presenting an adjusted p-value smaller than 0.05. Alternatively, we also studied the differences across the different treatments using the R package DESeq2(20), comparing the intercepts for every treatment in a negative binomial regression also accounting for the scaling factors from RUV-4 model. Using the differentially expressed genes in each comparison, we then performed enrichment analysis (GSEA) to

bioRxiv preprint doi: https://doi.org/10.1101/2024.11.07.622471; this version posted November 8, 2024. The copyright holder for this preprint (which was not certified by peer review) is the author/funder. All rights reserved. No reuse allowed without permission.

identify relevant biological pathways(21). To do so, we employed the "fry" method from the R package limma(19), using the canonical pathways gene sets from the Reactome pathway database(22). The results were then analyzed and visualized using the R package vissE(23).

Projection Approach for Data Visualization

We used the Statistical Quantile Learning (SQL) method(24), a tool for nonlinear dimensionality reduction, to summarize, analyze, and visualize adaptive and innate immunity data separately. We chose SQL due to its capability to handle high-dimensional datasets and accurately capture complex, nonlinear relationships often found in biological data. The adaptive immune panel featured cell subsets such as $CD20^{high}$, $CD20^{high}Ki67^{high}$, $CD20^{high}Ki67^{high}Bcl6^{high}$, $CD4^{high}$, $PD1^{high}$, $PD1^{high}Ki67^{high}$, $PD1^{high}CD57^{high}$, and $PD1^{high}Ki67^{high}Bcl6^{high}$. On the other hand, the innate immune panel included cell subsets like $CD8^{high}$, $CD8^{high}GrzB^{high}$, $CD14^{high}$, MPO^{high}, and $CD68^{high}$. These markers were specifically chosen to aid in clustering and classifying our immune data and extracted from our Histocytometry analysis. The SQL method provides a straightforward approach to estimating nonlinear latent variable models, or generative models. Unlike local methods such as UMAP, SQL assumes a probabilistic model and learns a generator, which is a smooth function that connects the laten space to the data space. This approach enables SQL to learn a global latent space that captures the overall structure of the data, whereas UMAP emphasizes preventing local neighborhood relationships. The generator allows for easy reconstruction of the data from the latent space, which permits interpretability of the latent space. Compared to other generative methods (such as Variational Autoencoders) SQL is not only easy to fit but also performs better for small samples and large-dimensional data. Additionally, SQL is supported by statistical guarantees and delivers unique and interpretable latent variables. This approach may therefore provide a reliable means to uncover insights that might be overlooked by other methods. Our goal was to cluster our three groups —RF-Bcl6no/low, RF-Bcl6int, and RF-Bcl6high— while also considering different age groups ("Aged" and "Young"). This methodology allowed for clearer separations and deeper insights into adaptive and innate immunity data across varied age groups and offers more meaningful insights, especially in understanding immune response variations within the specified groups.

For the spatial transcriptomic data, Principal Component Analysis (PCA) was employed to analyze specific gene sets across the section ROIs. This technique reduces the high-dimensional gene expression data into principal components that capture the most significant variance, facilitating a clearer visualization of patterns across the different ROI groups.

bioRxiv preprint doi: https://doi.org/10.1101/2024.11.07.622471; this version posted November 8, 2024. The copyright holder for this preprint (which was not certified by peer review) is the author/funder. All rights reserved. No reuse allowed without permission.

Statistical Analysis

Unpaired Non-Parametric Mann-Whitney t-test and Wilcoxon t-test were used for the analysis of mIF data, while a Mixed Effect Model was applied to the serological measurements, comprising fixed effects corresponding to various serological measurements and random effects originating from individual donors. Mean and standard deviation were calculated for normally distributed data, while median and interquartile range were reported for non-normally distributed data. A p value of less than 0.05 was considered significant, with significance levels indicated as follows: $p > 0.05$ (ns), $p \leq 0.05$ (*), $p \leq 0.01$ (**), $p \leq 0.001$ (***), and $p \leq 0.0001$ (****). Error bars on the graphs represent the mean with the standard error of the mean (SEM). FDR was applied for p value correction, with raw p values and FDR-adjusted p values, along with their significance symbols, reported for the main figures and for the supplementary figures **(Tables 6 and 7)**. The p values displayed on the graphs are derived from the raw P values. Graphs were generated using GraphPad Prism (version 8.3.0), Python (version 3.10.9), and R (version 4.3.0).

bioRxiv preprint doi: https://doi.org/10.1101/2024.11.07.622471; this version posted November 8, 2024. The copyright holder for this preprint (which was not certified by peer review) is the author/funder. All rights reserved. No reuse allowed without permission.

RESULTS

COVID-19 infection induces diverse and heterogeneous RF profiling in LD-LNs.

We started our investigation by analyzing F/GC B-cell subsets in LD-LNs from "Aged" (≥60 years) and "Young" (<57 years) individuals **(Tables 1 and 2)**, by applying a multiplex imaging assay **(Tables 3 and 4)** that allows for the simultaneous detection of CD20, Bcl6, and Ki67 **(Figures 1A and S1A)**. Follicular areas, identified by the density of $CD20^{high/dim}$ cells, were further analyzed for B cell subsets using Histocytometry analysis for all combined follicles (total follicular area-All F) **(Figure 1B)**. Through visual assessment of raw mIF images and quantitative analysis of the $Bcl6^{high}$ B cell counts, either per follicular area or total follicular area per tissue, we identified three distinct tissue subgroups: RF-Bcl6no/low, RF-Bcl6int, and RF-Bcl6high **(Figures 1C)**. Notably, the RF-Bcl6no/low group displayed Ki67 expression, indicating active proliferation and confirming these as RFs rather than primary or resting follicles. Furthermore, the area of individual RFs was significantly smaller in RF-Bcl6no/low tissues compared to those in the other two groups **(Figure 1D)**, while no significant differences were observed in other morphological features analyzed.

Next, the cell densities (normalized cell counts/per μm2) of specific B-cell subsets were calculated. Despite the similar cell density of bulk $CD20^{high/dim}$ B-cells across the three "Aged" subgroups, RF-Bcl6int and RF-Bcl6high tissues were characterized by significantly higher cell densities of proliferating $Ki67^{high}$ and $CD20^{high/dim}Ki67^{high}Bcl6^{high}$ B-cells **(Figure 1E)**. A similar profile was found when the frequency (%) or absolute cell counts of B-cell subsets **(Figure S1B)**. For the "Young" group, only a comparison between RF-Bcl6no/low and RF-Bcl6int subgroups could be applied. Although in "Aged" a significant difference was observed between RF-Bcl6no/low and RF-Bcl6int tissues in terms of bulk B-cell density, this difference did not reach significance when B-cell subsets were analyzed **(Figure 1E)**. A similar profile was observed when the frequency (% of total cells) or absolute cell counts of B-cell subsets were calculated **(Figure S1B)**.

Then, the pattern of the FDC network, as an additional surrogate of mature RFs, was also evaluated **(Figure S1C)**. We found a diverse expression of FDC in most RFs from both "Aged" RF-Bcl6no/low and RF-Bcl6high tissues. However, the FDC staining pattern varied between the two subgroups, with a connected network pattern more frequently observed in RF-Bcl6high tissues, while unconnected FDC positive events, a sign of less active follicles and mature RFs, were more commonly seen in RF-Bcl6no/low tissues **(Figure S1C)**. Altogether,

bioRxiv preprint doi: https://doi.org/10.1101/2024.11.07.622471; this version posted November 8, 2024. The copyright holder for this preprint (which was not certified by peer review) is the author/funder. All rights reserved. No reuse allowed without permission.

our data suggest that RFs, as indicated by the cell densities of Ki67^{high} and Bcl6^{high} B-cells, in LD-LNs from COVID-19-infected individuals are highly diverse and heterogeneous.

RF-Bcl6high LD-LNs harbor higher cell densities of proliferating Bcl6^{high} and CD57^{high} TFH cells.

Given the critical role of TFH-cells in the development and maintenance of GC-RFs(5), we aimed to analyze their *in-situ* cell densities in the three aforementioned subgroups. TFH-cell subsets were identified based on the expression of PD1, Bcl6, Ki67, and CD57, a marker that marks a distinct TFH-cell subset(25), (26) **(Figures 2A and B)**. We noticed an inconsistency in the co-expression of CD57 and CD4 in the RFs among individuals, possibly reflecting a downregulation of CD4 receptor, similar to CD3 expression pattern(25), in these highly differentiated TFH cells. Given this characteristic, we refined our gating strategy to avoid bias by identifying TFH-cells as PD1^{high} and PD1^{high}CD57^{high} **(Figure 2B)**. To set relevant cut-off values, we used PD1 and CD57 expression levels in extra-follicular (EF) CD4 T-cells as a reference and applied these thresholds to total F cells **(Figure 2B)**.

Calculation of absolute numbers of TFH-cells positive for Bcl6 in individual RFs revealed a similar profile to the one found for the B-cells (**Figure 2C**). A significantly higher cell density of PD1^{high}, PD1^{high}Ki67^{high}, PD1^{high}CD57^{high}, and PD1^{high}Ki67^{high}Bcl6^{high} cells in RF-Bcl6int and RF-Bcl6high compared to RF-Bcl6no/low tissues, in the "Aged" group, was observed **(Figure 2D)**. Despite the lack of statistical significance, the "Young" group exhibited a similar profile, with RF-Bcl6int showing significantly higher cell density of PD1^{high}Ki67^{high} and PD1^{high}CD57^{high} compared to RF-Bcl6no/low **(Figure 2D)**. A similar profile was found when the frequency (%) or absolute cell counts of TFH-cell subsets were analyzed **(Figure S1D)**. Then, we applied the SQL method(24) for clustering analysis of the tissues based on the B-cell and TFH-cell measurements. The SQL projection revealed a distinct clustering pattern for RF-Bcl6high compared to RF-Bcl6no/low and RF-Bcl6int subgroups **(Figure 2E)**. Altogether, our data show that the prevalence of Bcl6 in LD-LN from COVID-19 autopsies is associated with distinct RF immune landscaping.

The increasing prevalence of Bcl6 is associated with an altered spatial distribution of RF immune cell subsets.

Next, we analyzed the spatial distribution of key immune cell subsets within RFs in the "Aged" group by applying relevant algorithms to the RF-Bcl6int and RF-Bcl6high subgroups.

bioRxiv preprint doi: https://doi.org/10.1101/2024.11.07.622471; this version posted November 8, 2024. The copyright holder for this preprint (which was not certified by peer review) is the author/funder. All rights reserved. No reuse allowed without permission.

Although not significant, a positive correlation, between PD1^{high}CD57^{high} TFH-cells and CD20$^{high/dim}$Ki67^{high}Bcl6^{high} B-cells was found in the RF-Bcl6high subgroup **(Figure 3A)**. Furthermore, the ratio of CD20$^{high/dim}$Ki67^{high}Bcl6^{high} to PD1^{high}CD57^{high} cells was significantly higher in the RF-Bcl6high compared to the RF-Bcl6int subgroup **(Figure 3B)** suggesting a higher possibility for B/T cell interaction in the RF-Bcl6high subgroup. Then, the X, and Y coordinates of individual cells (CD20$^{high/dim}$Ki67^{high}, CD20$^{high/dim}$Ki67^{high}Bcl6^{high}, PD1^{high}CD57^{low} and PD1^{high}CD57^{high} cells) were extracted, focusing only on RFs containing at least 20 cells of the corresponding phenotypes. Using G-Function analysis **(Figures 3C and S2A)**, we found a significantly less scattered distribution for CD20$^{high/dim}$Ki67^{high} B cells in the RF-Bcl6high compared to RF-Bcl6int tissues **(Figure 3D, upper left panel)** while the PD1^{high} TFH-cells, from the same RFs areas, exhibited the opposite profile **(Figure 3D, upper right panel)**. Then, RF areas were analyzed considering their Bcl6 reactivity. CD20$^{high/dim}$Ki67^{high}Bcl6^{high} B-cells displayed a significantly less scattered/higher clustering profile in tonsils compared to RF-Bcl6int and RF-Bcl6high tissues **(Figure 3D, lower left panel)**. This was also the case for PD1^{high}CD57^{high} TFH-cells between tonsils and RF-Bcl6high LNs **(Figure 3D, lower right panel)**. Distance matrix analysis **(Figure 3E)** revealed a similar mean minimum Euclidean distances between proliferating CD20$^{high/dim}$Ki67^{high} B-cells and PD1^{high}CD57^{low} TFH-cells **(Figure 3F, left panel)** and a clear trend (p= 0.0784) for shorter distance between CD20$^{high/dim}$Ki67^{high} B-cells and PD1^{high}CD57^{high} TFH-cells **(Figure 3F, middle panel)** in RF-Bcl6high compared to RF-Bcl6int subgroup. However, no difference was found between CD20$^{high/dim}$Ki67^{high}Bcl6^{high} and PD1^{high}CD57^{high} TFH-cells **(Figure 3F, right panel)**. Altogether, our findings suggest that between the RF-Bcl6int to RF-Bcl6high stage, there is a notable shift in the spatial organization of key immune cell subsets, with increased clustering of proliferating CD20$^{high/dim}$Ki67^{high} B-cells and presumably higher possibility for their interaction with PD1^{high}CD57^{high} TFH-cells in the RF-Bcl6high "Aged" subgroup of LD-LNs.

COVID-19 infection reveals a disconnection in RF immunoreactivity between LD-LNs and matched distal subdiaphragmatic LNs.

We analyzed LD-LN and subdiaphragmatic (SD-LNs, serving as "control") LNs from the same donors (**Table 5**) in the "Aged" group to investigate whether COVID-19 infection leads to a generalized RFs Bcl6 immunoreactivity. The adaptive immunity panel **(Table 3)** was applied to the SD-LNs **(Figure 4A)**. Overall, a trend for lower cell densities of B-cell and TFH-cell subsets that reached significance for the CD20$^{high/dim}$Ki67^{high}Bcl6^{high} cell subset in the SD-

bioRxiv preprint doi: https://doi.org/10.1101/2024.11.07.622471; this version posted November 8, 2024. The copyright holder for this preprint (which was not certified by peer review) is the author/funder. All rights reserved. No reuse allowed without permission.

LNs compared to LD-LNs was found **(Figure 4B)**. Consistent with this profile, SD-LNs showed a significantly lower frequency of $CD20^{high/dim}Ki67^{high}Bcl6^{high}$, $PD1^{high}Ki67^{high}$, and $PD1^{high}Ki67^{high}Bcl6^{high}$ cells compared to LD-LNs **(Figure 4C)**. Therefore, the generalized inflammation associated with COVID-19 infection may not trigger the development of RF Bcl6 immune reactivity in distal, non-LD-LNs.

Contrary to B/TFH combined profile, LD-LNs RF-Bcl6high reactivity is not associated with a distinct CD8/innate immunity profile.

Next, we investigated the prevalence of bulk and effector $GrzB^{high}$ $CD8^{high}$ T-cells, as well as innate immunity subsets (CD68, CD14 for monocytes/macrophages, and MPO, a marker of granulocytes) (**Figures 5A and S2B)**. The antibody panel **(Tables 3 and 4)** did not include follicular markers, so our Histocytometry analysis applied to both follicular (F) and extrafollicular (EF) areas **(Figure 5B)**. Similar cell densities of $CD8^{high}$ and $CD8^{high}GrzB^{high}$ cells were found among the three tissue subgroups, for both "Young" and "Aged" individuals **(Figure 5C, left panels)**. In contrast to $CD8^{high}$ T-cells, a mixed profile was observed when innate immunity cell types were analyzed. Significantly higher numbers of MPO^{high} and $CD68^{high}$ cells were found in RF-Bcl6high compared to either RF-Bcl6int or RF-Bcl6no/low "Aged" donors (**Figure 5C, right panels)**. The comparison between matched subgroups showed significantly increased numbers of MPO^{high}, $CD68^{high,}$ and $CD14^{high}$ cells in "Young" compared to "Aged" donors **(Figure 5C, right panels)**. Then, a SQL analysis based on the CD8, and innate immune cell subsets was applied. No distinct profile was found between the RF-Bcl6 subgroups, regardless of the aging **(Figure 5D)**. Thus, COVID-19 infection results in a relatively homogenous cell density profile of CD8/innate immunity cell types in LD-LNs regardless of their Bcl6 reactivity.

The possible association between serological measurement at different time points and RF-Bcl6 reactivity was investigated **(Figures 5E and S2C)**. To this end, a mixed linear regression model analysis was performed. A trend for higher levels of CRP was observed in RF-Bcl6high compared to RF-Bcl6no/low subgroup ($\beta = 61.657$, $p = 0.064$). No difference was found when leukocyte and lymphocyte counts were analyzed among the subgroups **(Figures 5E and S2C)**. Analysis of the ratio between LD-LN MPO^{high} cells and circulating granulocytes (neutrophils, basophils, eosinophils) showed a significantly higher ratio in RF-Bcl6high compared to RF-Bcl6int subgroup **(Figure 5F)**. Next, we sought to investigate whether RF-Bcl6 reactivity was (or not) associated with the estimated time after infection (based on days of hospitalization). No significant association was found in all three subgroups ($p = 0.857$, $p = 0.1$,

bioRxiv preprint doi: https://doi.org/10.1101/2024.11.07.622471; this version posted November 8, 2024. The copyright holder for this preprint (which was not certified by peer review) is the author/funder. All rights reserved. No reuse allowed without permission.

and p = 0.859 for the RF-Bcl6no/low, RF-Bcl6int group, and RF-Bcl6high group respectively) **(Figure 5G)**. A similar profile was observed when the RF-Bcl6 expression over time was analyzed for "Aged" and "Young" donors separately **(Figure S2D)**. Our data suggest that the observed heterogeneity of LD-LN RF-Bcl6 reactivity may reflects the intrinsic capacity of the immune system to mount mature GC-RFs rather than a profile associated with the time of autopsy post-infection.

The RF-Bcl6high tissues are characterized by a distinct *in situ* follicular transcriptomic profile.

The GeoMx platform was applied to RF areas from tissues spanning the three subgroups, using normalized and batch-corrected data for analysis (**Figures S3A and S3B**). Principal Component Analysis (PCA) revealed distinct transcriptional profiles among RF areas based on Bcl6 expression **(Figure 6A)**. Given the tissue unavailability, we were not able to compare the *in situ* transcriptomic profiling between "Young" and "Aged" RF-Bcl6high groups. We focused our subsequent analysis on the "Aged" group by comparing RF-Bcl6no/low and RF-Bcl6int subgroups to the RF-Bcl6high one. Several differentially expressed genes (DEGs) emerged from the RF-Bcl6no/low vs. RF-Bcl6high comparison, with genes promoting GC-development (e.g. Bcl6, AICDA, IL21R, CXCL13, STAT3) overexpressed in RF-Bcl6high, while genes associated with a TH1-immune response (e.g. STAT4, TNFRSF10B, TNFRSF1A, CXCR3, TGFB3, IL7) were significantly upregulated in the RF-Bcl6no/low group **(Figures 6B and 6C)**. Analysis of the distribution "profile" of these gene sets among the RFs (ROIs) of a given tissue, showed a denser clustering for the "TH1-favoring" gene set in the RF-Bcl6no/low subgroup, compared to the more scattered profile for the "GC-favoring" gene set in the RF-Bcl6high subgroup **(Figures S3C and S4A)**. The comparison between RF-Bcl6int and RF-Bcl6high "Aged" subgroups revealed a significant upregulation of genes favoring TFH/GC formation (e.g. CXCL13, CD22, MIF, STAT3, AICDA) in the RF-Bcl6high group **(Figure 6D)**. The gradual upregulation of GC-promoting genes, such as AICDA, Bcl6, and STAT3, from RF-Bcl6no/low to RF-Bcl6int to RF-Bcl6high highlights the progressive development of maturing GC-RFs activity across these subgroups **(Figure 6E)**. Despite the consistent downregulation of genes associated with a TH1 response in the RF-Bcl6high compared to the RF-Bcl6no/low subgroup, a mixed profile was observed when the RF-Bcl6int subgroup was analyzed **(Figure 6E)**.

Pathway enrichment analysis revealed upregulation of TNF-related pathways (e.g. "TNFR1 Signaling", "NF-kappa-B Signaling", "TRAIL Signaling") and interferon pathways

bioRxiv preprint doi: https://doi.org/10.1101/2024.11.07.622471; this version posted November 8, 2024. The copyright holder for this preprint (which was not certified by peer review) is the author/funder. All rights reserved. No reuse allowed without permission.

(e.g. “Alpha/Beta Interferon Signaling”) in follicles from “Aged” RF-Bcl6no/low compared to RF-Bcl6high tissues **(Figure 7A)**. Conversely, pathways related to metabolism, DNA repair, and immune activation (e.g. “Respiratory Electron Transport”, “ATP Synthesis”, “Mismatch Repair”) were significantly enriched in the RF-Bcl6high group. The “Aged” RF-Bcl6high subgroup also showed upregulation of RF-development pathways (e.g. “IL4”, “IL6 signaling”, “detoxification of reactive oxygen species”) compared to the “Aged” RF-Bcl6int subgroup **(Figure S4B)**.

The differential expression analysis between “Young” and “Aged” RF-Bcl6no/low tissues revealed the upregulation of TNF-family genes (e.g. TNFSF10, TNFRSF1A, TNFRSF12A, TNFRSF10C) in the “Aged” group, indicating an enhanced pro-inflammatory environment **(Figure 7B)**. Pathway analysis supported this **(Figure 7B, left panel)**, further showing increased activation of interferon signaling pathways, crucial for driving inflammatory responses **(Figure 7B, right panel)**. Comparing “Young” and “Aged” RF-Bcl6int groups, the “Young” subgroup displayed upregulation of immune-related genes (e.g. IL4R, CD22, TNFRSF14), pointing to a more “reactive” immune environment, while the “Aged” subgroup exhibited higher expression of genes related to GC reactivity (AIDA, MIF, CXCL13, CXCR4) **(Figure 7C)**. Our “Young” RF-Bcl6no/low group included two different LD-LNs (24-a/24-b) from the same donor and anatomical site (mediastinal). No difference was observed in terms of DEGs or enriched pathways between these two LD-LNs (**Figure S4C**). Furthermore, the same group included one distal (axillary) LN, allowing for the comparison to the rest of the LD-LNs within the same (RF-Bcl6no/low) group **(Figure S4D)**. We observed several DEGs as well as an upregulation of pathways related to interleukin signaling (IL-7, IL-15, and IL17) and extracellular matrix organization in the axillary compared to LD-LNs **(Figure S4D)**. Therefore, the development (or not) of RF-Bcl6 reactivity in COVID-19 LD-LNs is associated with a distinct *in situ* molecular profiling that could be affected by aging.

“Aged” RF-Bcl6no/low tissues are characterized by a distinct *in situ* follicular macrophage profile.

Given the potential role of the aforementioned inflammatory pathways for the development of RFs in COVID-19, we aimed to further characterize the profile of macrophages in our tissue cohort. To this end, a set of genes from our GeoMx analysis was selected based on their macrophage “specificity” (including function-related genes like IL12B, CXCL9, and

bioRxiv preprint doi: https://doi.org/10.1101/2024.11.07.622471; this version posted November 8, 2024. The copyright holder for this preprint (which was not certified by peer review) is the author/funder. All rights reserved. No reuse allowed without permission.

CCL7) and their expression was compared among different tissue subgroups. A significant upregulation of all selected genes was observed in the "Aged" RF-Bcl6no/low subgroup compared to the "Aged" RF-Bcl6high group **(Figure 8A)** while that was also true for a subset of the genes when a comparison to the "Young" RF-Bcl6no/low group was applied **(Figure 8B)**. Of note, we also found a significant (p=0.0069) association between the prevalence of $CD68^{high}$ cells and death post-infection (DPI) only in the "Aged" RF-Bcl6no/low subgroup **(Figure 8C, left panel)**. A clear trend (p=0.066) was found for the $CD14^{high}$ cell too **(Figure 8C, right panel)**. Therefore, our data indicate qualitative differences of the RF macrophages in the COVID-19 LD-LN with respect to Bcl6 reactivity.

bioRxiv preprint doi: https://doi.org/10.1101/2024.11.07.622471; this version posted November 8, 2024. The copyright holder for this preprint (which was not certified by peer review) is the author/funder. All rights reserved. No reuse allowed without permission.

Discussion

Given the lack of accessibility to relevant human LNs, the cellular and molecular mechanisms regulating the follicular/germinal center immune dynamics in draining LNs during viral infections, particularly during the early phase— the initial period following viral exposure when the immune response is first activated—are poorly understood. Here, we leveraged the availability of LD-LNs and matched control distal LNs from COVID-19 autopsies to investigate the RFs' immune landscaping and the molecular pathways active *in situ* with a focus on the impact of donor aging. The "Young" group included only one RF-Bcl6high LD-LN, challenging the analysis between "Young" and "Aged" donors for this subgroup.

We stratified LD-LNs into three distinct subgroups based on Bcl6 expression levels to assess RF dynamics and activity. Analyzing the RFs based on $CD20^{high/dim}$ expression, we detected Ki67 expression, indicating active proliferation and confirming these structures as secondary follicular areas rather than primary, resting follicles in all tissues analyzed. The three subgroups (RF-Bcl6no/low, RF-Bcl6int, and RF-Bcl6high) were defined by varying levels of Bcl6 expression. Analysis of individual RFs in the RF-Bcl6int and RF-Bcl6high subgroups revealed substantial variability in Bcl6 expression, even within the same tissue or donor. The RF-Bcl6no/low subgroup was characterized by i) significantly smaller RFs areas, ii) the presence of proliferating B-cells ($CD20^{high/dim}Ki67^{high}$), although at significantly lower levels than in the other two subgroups, and iii) a distinct FDC staining pattern(27) that further highlighted these structures as reactive, less matured rather than resting follicles. Additionally, we observed inconsistent co-expression of CD4 and CD57 in the RFs, likely due to CD4 downregulation in $PD1^{high}CD57^{high}$ TFH cells. Therefore, we chose to analyze total $PD1^{high}CD57^{high}$ and $PD1^{high}CD57^{low}$ cells within the RFs as a surrogate marker for TFH cells. The significantly higher PD1 expression in RFs versus extrafollicular areas, along with the significantly lower PD1 expression in extrafollicular and follicular $CD8^{high}$ T-cells compared to TFH cells(28), suggests that our approach would not lead to miscalculation of TFH cells. Taking into consideration the calculated B and CD4 T-cell subsets, a distinct clustering of RF-Bcl6high tissues was observed. This clustering was less evident between RF-Bcl6no/low and RF-Bcl6int tissues, possibly reflecting an intermediate stage of germinal center development in the RF-Bcl6int subgroup. Overall, our data revealed a balanced representation of the three RF subgroups based on Bcl6 expression in COVID-19-infected individuals.

bioRxiv preprint doi: https://doi.org/10.1101/2024.11.07.622471; this version posted November 8, 2024. The copyright holder for this preprint (which was not certified by peer review) is the author/funder. All rights reserved. No reuse allowed without permission.

Next, we sought to investigate the spatial positioning of CD4 and B-cell subsets in RF-Bcl6int and RF-Bcl6high LD-LNs from "Aged" donors. Despite the similar cell densities of $CD20^{high/dim}Ki67^{high}$ and $PD1^{high}$ cells among the two subgroups, their distribution/scattering profile was different. The $PD1^{high}CD57^{high}$ phenotype marks a unique TFH subset with a distinct function, positioning (closer to Dark Zone compared to $PD1^{high}CD57^{low}$ TFH cells (25)), and molecular profile(29), (30), (25). A clear trend for closer proximity of $PD1^{high}CD57^{high}$ TFH to $CD20^{high/dim}$ $Ki67^{high}$ B cells was observed in RF-Bcl6high tissues compared to RF-Bcl6int tissues. Assuming that the distance between two cells reflects the likelihood of their interaction, these findings suggest an increased possibility for B/T cell interactions in the RF-Bcl6high subgroup. The ratio and spatial positioning profile of B-cell and TFH-cell subsets further supports our hypothesis that the RF-Bcl6int phenotype may represent a transitional or less mature stage of RF development compared to the more established RF-Bcl6high phenotype.

The direct comparison between LD-LNs and matched subdiaphragmatic, distal LNs, suggests that despite the systemic inflammation/immune activation associated with COVID-19 and the possible dissemination of the virus at different anatomical sites across the human body(31), COVID-19 infection can induce mature RFs immune reactivity selectively in regional/draining lymphoid organs. The formation of Tertiary Lymphoid Structures (TLS) in long COVID-19 was recently described(32). Whether the development of a RF-Bcl6high reactivity in LD-LNs is also associated with the presence of lung-associated TLS, in our cohort, remains to be determined.

In situ analysis of bulk and effector ($GrzB^{high}$) CD8 T-cells revealed a similar profile across the groups, irrespective of aging. Contrary to B-cells and T-cells, clustering analysis considering CD8, and innate cell types showed a more homogeneous profile among the RF-Bcl6 groups, likely reflecting a generalized inflammatory LN environment characteristic in COVID-19 infection. Among the serum measurements, CRP was found significantly higher in RF-Bcl6high compared to RF-Bcl6no/low tissues. This profile, however, was not associated with lymphopenia or higher circulating numbers of neutrophils, a hyperinflammation profile previously described in COVID-19(33). The higher ratio of LN MPO / circulating granulocytes found in RF-Bcl6high tissues may represent a higher extravasation of this cell type to LD-LNs. Most importantly, our modeling analysis revealed that the Bcl6 cell density in LD-LNs is not associated with the time of death post-infection (DPI) suggesting that the intrinsic ability of the immune system of a given individual and *in situ* operating biological factors are responsible for

bioRxiv preprint doi: https://doi.org/10.1101/2024.11.07.622471; this version posted November 8, 2024. The copyright holder for this preprint (which was not certified by peer review) is the author/funder. All rights reserved. No reuse allowed without permission.

the observed phenotypes rather than the lack of adequate time for the development of RF-Bcl6int/high reactivity.

The spatial follicular transcriptomic profiling showed distinct molecular signatures associated with the level of RF-Bcl6 expression in "Aged" lymph node (LD-LN) tissues. Previous studies, using bulk LN mRNA preparation, have attributed the absence of Bcl6 expression in COVID-19 hilar LNs to overexpression of TNF-related genes, specifically TNF-α(6), which impaired the development of TFH cells. Our data extend these findings by showing that compromised Bcl6 expression in LD-LNs is associated with significantly increased expression of genes and pathways favoring TH1 differentiation within the follicular/GC areas. Specifically, genes counteracting TFH-development, such as KLF2(34), STAT4(35), STAT5A/B(36), IFNAR1, and TGFB3(37), as well as those characterizing or favoring a TH1-response, including CXCR3 and TNF-related genes (TNF-receptors like TNFRSF1A (DR1), TNFRSF25 (DR3), and TNFRSF10B (DR5), and TNF-signaling mediators like TRAF2). Additionally, other key genes involved in TNF-signaling, such as TNFRSF1B (TNFR2) and TNFRSF10C (DcR1), contribute to the regulation of immune responses and apoptosis pathways, were overexpressed in RF-Bcl6no/low compared to RF-Bcl6high tissues. Conversely, the RF-Bcl6high phenotype was supported by significant increases in genes favoring B/TFH cell development (e.g. BCL6, AICDA, CD74, STAT3), their trafficking (e.g. CXCL13, CXCR4, S1PR), T-cell development (TCF3), and pathways like "Antigen BCR activation" and "TCF-dependent signaling". Therefore, our imaging data, coupled with transcriptomic analysis, suggest that high Bcl6 cell density is possibly associated with the coordinated expression and function of several cell subsets and molecular pathways favoring GC development. On the other hand, the RF-Bcl6int profile was characterized by an intermediate expression of genes favoring GC development and a mixed expression profile of TH1-favoring genes. These findings further support the hypothesis that RF-Bcl6int phenotype represents a transitional stage of GC development, in line with the aforementioned B-cell and T cell-based clustering profiles and neighboring analysis.

Our imaging data point to an overall trend for higher cell densities of macrophage/monocytes in RF-Bcl6high compared to RF-Bcl6no/low tissues. However, the expression pattern of macrophage function-related genes suggests an elevated capacity of macrophages for stimulation (expression of TLR3) and production of cytokines/chemokines, in the RF-Bcl6no/low subgroup. Furthermore, the modeling analysis revealed an accumulation of CD68 and CD14 over time DPI only in the RF-Bcl6no/low subgroup. Our data are in line with

bioRxiv preprint doi: https://doi.org/10.1101/2024.11.07.622471; this version posted November 8, 2024. The copyright holder for this preprint (which was not certified by peer review) is the author/funder. All rights reserved. No reuse allowed without permission.

previous findings showing that elevated TNF-α production in COVID-19 LNs contributes to the loss of GC Bcl6 reactivity(6). Therefore, the quality of macrophages, the primary producers of TNF-α(38), could play a critical role in the development of GCs during early viral infections. Further, we observed upregulation of certain macrophage function-related genes in “Aged” RFs areas, likely in response to chronic low-grade inflammation, often referred to as "inflammaging”, which might reflect the heightened inflammatory environment in aging lymph nodes(39). These findings highlight the crucial role the macrophages could play in shaping the aging germinal center microenvironment and modulation of pathogen-specific B-cell responses.

We should also highlight the limitations of the current study including the absence of “non-infected control tissues” as well as the lack of data on antibody responses (titers or affinity). Whether the described RF-Bcl6 profile is linked to the development of anti-COVID-19 antibody responses, particularly those of high-affinity, cannot be addressed by the current study. However, our study provides cellular and molecular profiles, associated with the human F/GC development, that could fuel future investigation aiming to further understand the F/GC immune landscaping and model the development of B-cell responses in health and disease(40). This is of particular interest for the early phase of viral infections where accessibility to relevant LNs is highly challenging if possible.

https://doi.org/10.1101/2024.11.07.622471 ... ight holder for this ... out permission.

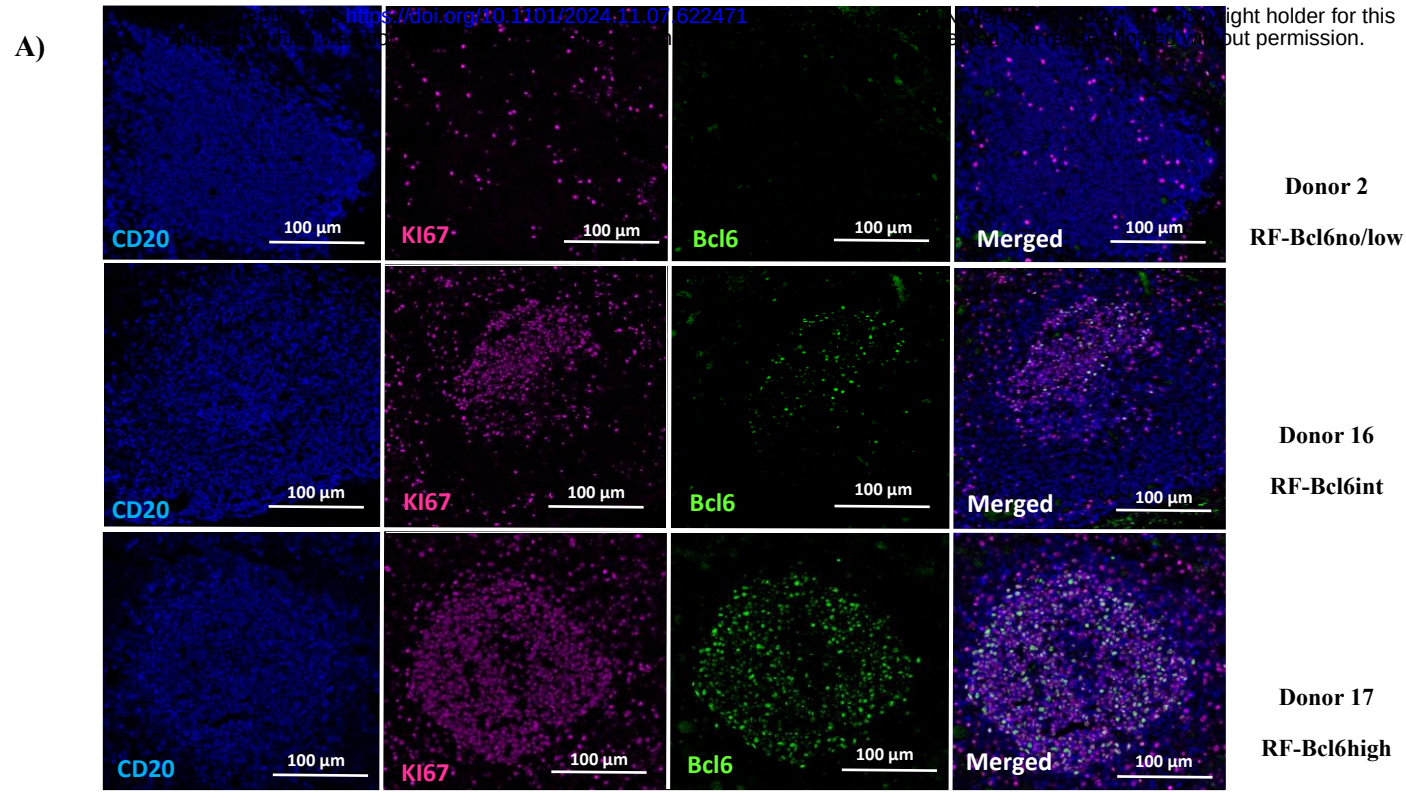

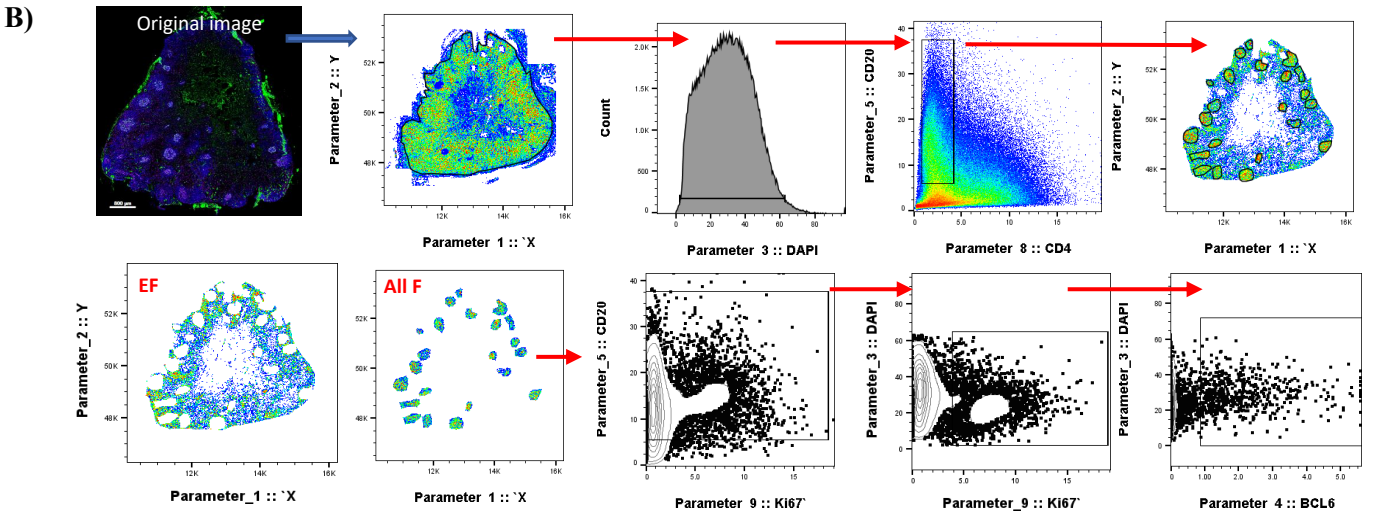

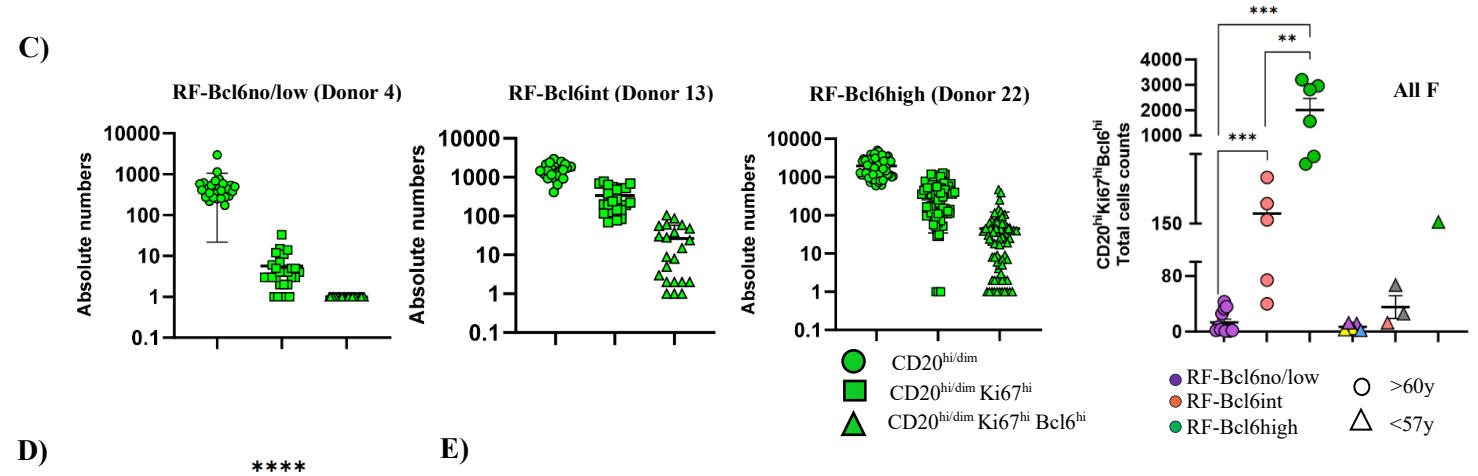

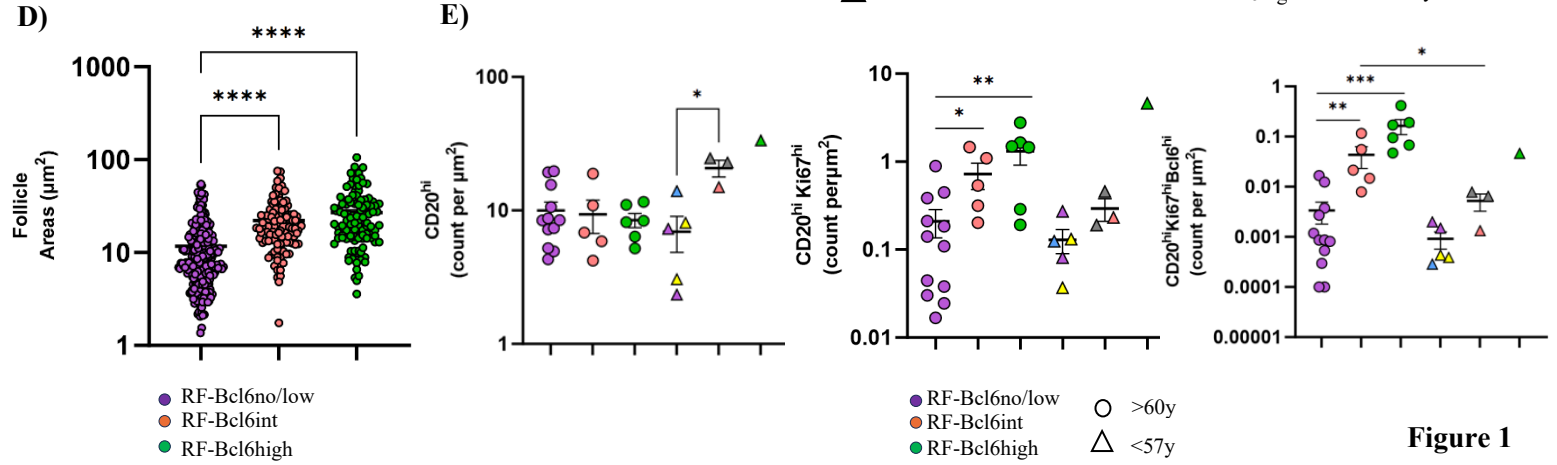

Figure 1

bioRxiv preprint doi: https://doi.org/10.1101/2024.11.07.622471; this version posted November 8, 2024. The copyright holder for this preprint (which was not certified by peer review) is the author/funder. All rights reserved. No reuse allowed without permission.

Figure 1. COVID-19 infection induces diverse and heterogeneous reactive follicles in LD-LNs. A) Representative fluorescence images (100µm) showing a follicular area in a RF-Bcl6no/low tissue (top images, donor 2), RF-Bcl6int tissue (middle images, donor 16), and in a RF-Bcl6high tissue (bottom images, donor 17) ($CD20^{high}$-blue, $Ki67^{high}$-magenta, $Bcl6^{high}$-green, and a merged image). **B)** The gating scheme (Histocytometry) for the identification of B cell subsets is shown. Follicular areas were identified based on the density of $CD20^{high/dim}$. The prevalence of B-cell subsets was calculated for all follicles combined (All F). **C)** Dot plot graphs showing the counted absolute numbers of B cell subsets ($CD20^{high/dim}$, $CD20^{high/dim}Ki67^{high}$, $CD20^{high/dim}Ki67^{high}Bcl6^{high}$) in three different donors (Donor 4 RF-Bcl6no/low, Donor 13 RF-Bcl6int and Donor 22 RF-Bcl6high), per follicle as well as for the total follicular area (All F, right panel). **D)** Dot plot graph of the calculated area of individual follicles normalized per tissue for RF-Bcl6no/low (purple), RF-Bcl6int (pink), and RF-Bcl6high (green) groups. **E)** Dot plot graphs showing the cell densities (normalized per μm^2 cell counts) of B-cell subsets ($CD20^{high/dim}$, $CD20^{high/dim}Ki67^{high}$, and $CD20^{high/dim}Ki67^{high}Bcl6^{high}$) in the three groups for the "Aged" (round marks) and "Young" (triangle marks) individuals. Within the "Young" RF-Bcl6no/low group; the blue triangle depicts an axillary Lymph node (donor 25), and yellow triangles depict para-aortic and mediastinal lymph nodes from the same donor (donor 29). Within the "Young" RF-Bcl6int group, two different Mediastinal lymph nodes from the same donor (donor 24-a and donor 24-b) are depicted by the grey triangles. Asterisks denote p-value: * $P \leq 0.05$, ** $P \leq 0.01$, and *** $P \leq 0.001$ (Unpaired Non-Parametric Mann-Whitney T-Test).

bioRxiv preprint doi: https://doi.org/10.1101/2024.11.07.622471; this version posted November 8, 2024. The copyright holder for this preprint (which was not certified by peer review) is the author/funder. All rights reserved. No reuse allowed without permission.

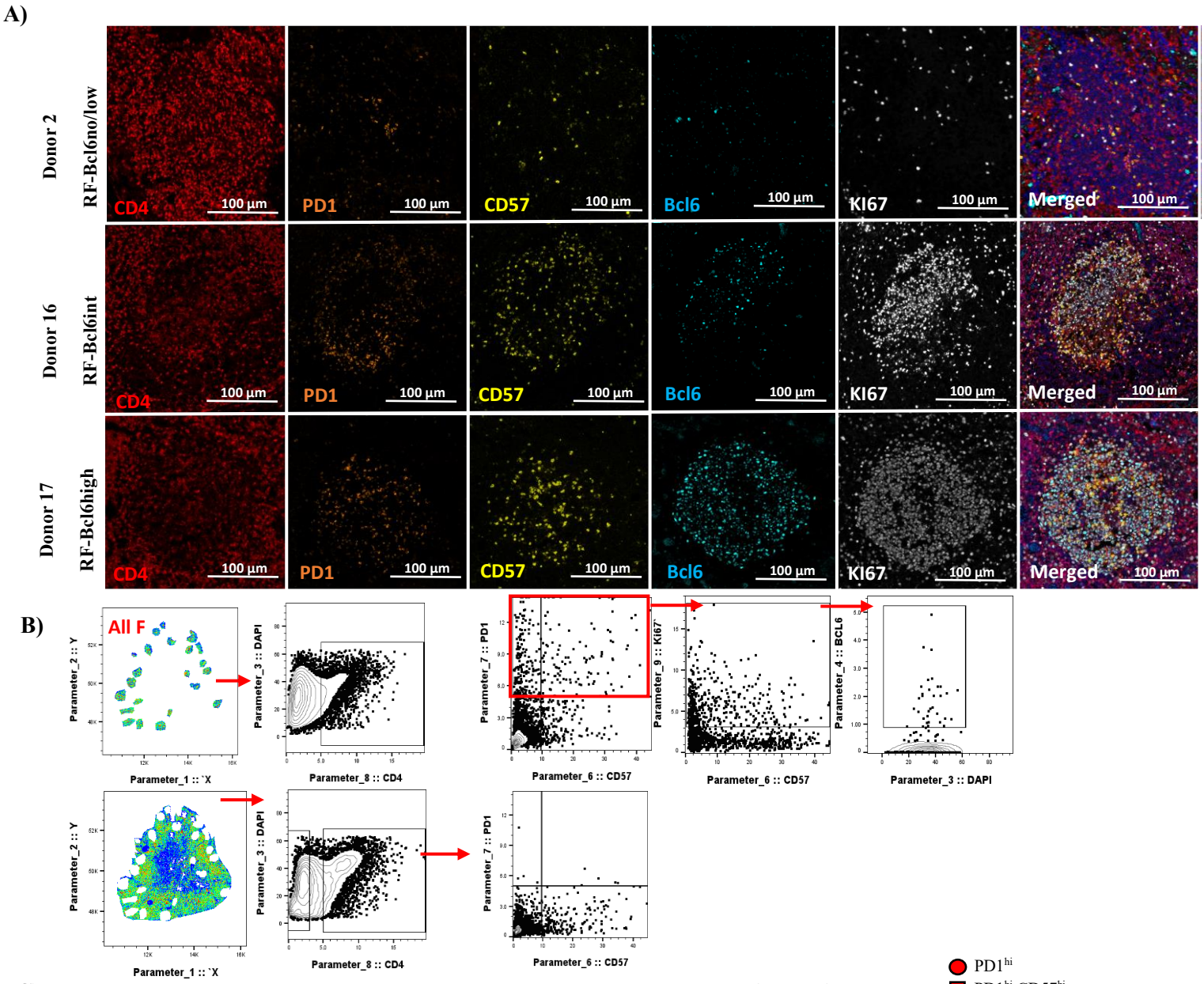

Figure 2

bioRxiv preprint doi: https://doi.org/10.1101/2024.11.07.622471; this version posted November 8, 2024. The copyright holder for this preprint (which was not certified by peer review) is the author/funder. All rights reserved. No reuse allowed without permission.

Figure 2. RF-Bcl6high LD-LNs harbor higher cell densities of proliferating Bcl6^{high} and CD57^{high} TFH cells. A) Representative fluorescence image (100 µm) showing a follicular area in a RF-Bcl6no/low tissue (left images, donor 2), RF-Bcl6int (middle image, donor 16), and a RF-Bcl6high tissue (right images, donor 17) (CD4^{high}-red, PD1^{high}-orange, CD57^{high}-yellow, Bcl6^{high}-cyan, Ki67^{high}-white, and a merged image). **B)** The gating scheme for the identification of CD4 T cell subsets is shown. Follicular areas were identified by the expression of CD20$^{high/dim}$. The prevalence of T cell subsets was calculated for all follicles combined (All F). **C)** Dot plot graphs showing the counted absolute numbers of T cell subsets (PD1^{high}, PD1^{high}CD57^{high}, PD1^{high}Ki67^{high}, PD1^{high}Ki67^{high}Bcl6^{high}) in three different donors (Donor 4 RF-Bcl6no/low, Donor 13 RF-Bcl6int and Donor 22 RF-Bcl6high) per follicle. **D)** Dot plot graphs showing the normalized (per µm^2) counts of T cell subsets (PD1^{high}, PD1^{high}Ki67^{high}, PD1^{high}CD57^{high} and PD1^{high}Ki67^{high}Bcl6^{high}) in the three groups for the "Aged" (round marks) and "Young" (triangle marks) individuals. Within the "Young" RF-Bcl6no/low group; the blue triangle depicts an axillary Lymph node (donor 25), and yellow triangles depict para-aortic and mediastinal lymph nodes from the same donor (donor 29). Within the "Young" RF-Bcl6int group, two different Mediastinal lymph nodes from the same donor (donor 24-a and donor 24-b) are depicted by the grey triangles. Asterisks denote p-value: * $P \leq 0.05$, ** $P \leq 0.01$, and *** $P \leq 0.001$(Unpaired Non-Parametric Mann-Whitney T-Test). **E)** SQL method clustering showing the projection of the different B cells and T cells subsets (adaptive immunity panel) based on CD20$^{high/dim}$, CD20$^{high/dim}$Ki67^{high}, CD20$^{high/dim}$Ki67^{high}Bcl6^{high}, CD4^{high}, PD1^{high}, PD1^{high}Ki67^{high}, PD1^{high}CD57^{high} and PD1^{high}Ki67^{high}Bcl6^{high} cell counts in the three groups (RF-Bcl6no/low in purple, RF-Bcl6int in pink and, RF-Bcl6high in green), for the "Aged" (round marks) and "Young" (triangle marks).

bioRxiv preprint doi: https://doi.org/10.1101/2024.11.07.622471; this version posted November 8, 2024. The copyright holder for this preprint (which was not certified by peer review) is the author/funder. All rights reserved. No reuse allowed without permission.

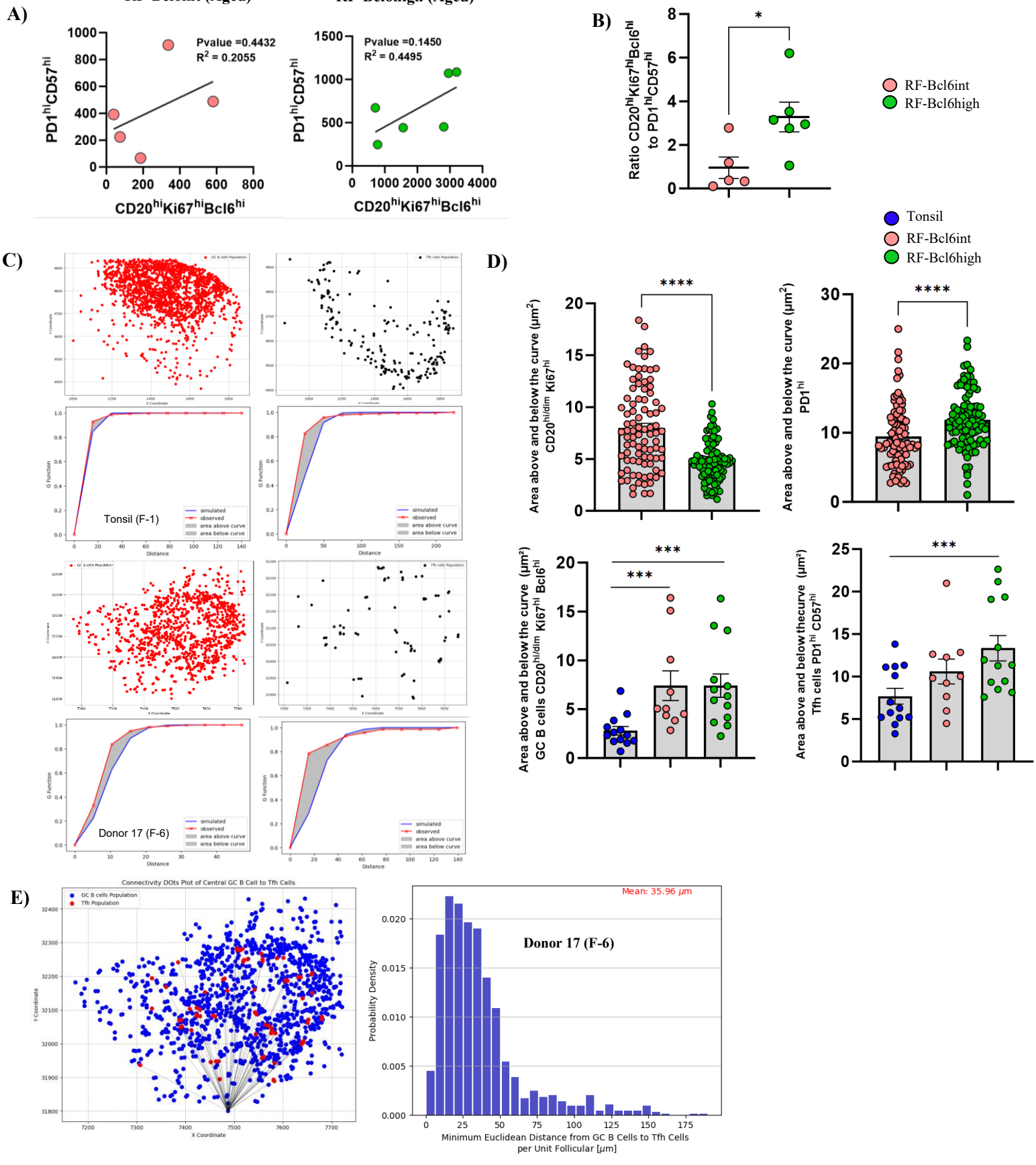

Figure 3

bioRxiv preprint doi: https://doi.org/10.1101/2024.11.07.622471; this version posted November 8, 2024. The copyright holder for this preprint (which was not certified by peer review) is the author/funder. All rights reserved. No reuse allowed without permission.

Figure 3. The increasing prevalence of Bcl6 is associated with an altered spatial distribution of RF immune cell subsets. A) Correlation analysis between $PD1^{high}CD57^{high}$ and $CD20^{high/dim}Ki67^{high}Bcl6^{high}$ in "Aged" RF-Bcl6int (upper left), and "Aged" RF-Bcl6high (upper right) **B)** Ratio analysis of $CD20^{high/dim}Ki67^{high}Bcl6^{high}$ to $PD1^{high}CD57^{high}$ cell counts in LD-LNs of "Aged" RF-Bcl6int (pink dots) and RF-Bcl6high (green dot); statistical analysis has been performed by Unpaired Non-Parametric Mann-Whitney T-Test. **C)** Graphs showing the distribution pattern of $CD20^{high/dim}Ki67^{high}$ (red) and $PD1^{high}CD57^{high}$ (black) cells in a control tonsil (top images, Tonsil F-1) and a RF-Bcl6high tissue (bottom images, Donor 17 F-6). Their corresponding G-Function graphs, showing the proximity of the G curve (red curve) to the theoretical curve (Poisson curve, blue curve), are shown too. The shade gray area represents the area between the two curves measured. **D)** Dot plot graphs of the measured area between the G and estimate curve for $CD20^{high/dim}Ki67^{high}$, $PD1^{high}$, $CD20^{high/dim}Ki67^{high}Bcl6^{high}$ and $PD1^{high}CD57^{high}$ for tonsils (blue dots), RF-Bcl6int (pink dots) and RF-Bcl6high (green dots) tissues. Asterisks denote p-value: * $P \leq 0.05$, ** $P \leq 0.01$, and *** $P \leq 0.001$ (Unpaired Non-Parametric Mann-Whitney T-Test). **E)** Connectivity dot plot identifying cell coordinates and distance measurements from $CD20^{high/dim}Ki67^{high}Bcl6^{high}$ (blue dots) to $PD1^{high}CD57^{high}$ (red dots) cells in a follicular area of a RF-Bcl6high tissue (Donor 17 F-6). The corresponding bar graph shows the distribution of cells based on the distance from $CD20^{high/dim}Ki67^{high}Bcl6^{high}$ to $PD1^{high}CD57^{high}$ cells. **F)** Dot plot graphs showing the mean of the minimum Euclidean distance measured from $CD20^{high/dim}Ki67^{high}$ to $PD1^{high}CD57^{low}$ or $PD1^{high}CD57^{high}$ and from $CD20^{high/dim}Ki67^{high}Bcl6^{high}$ to $PD1^{high}CD57^{high}$ cells, in several follicular areas of RF-Bcl6int (pink dots) and RF-Bcl6high (green dots) tissues. Asterisks denote p-value: * $P \leq 0.05$, ** $P \leq 0.01$, and *** $P \leq 0.001$(Unpaired Non-Parametric Mann-Whitney T-Test).

bioRxiv preprint doi: https://doi.org/10.1101/2024.11.07.622471; this version posted November 8, 2024. The copyright holder for this preprint (which was not certified by peer review) is the author/funder. All rights reserved. No reuse allowed without permission.

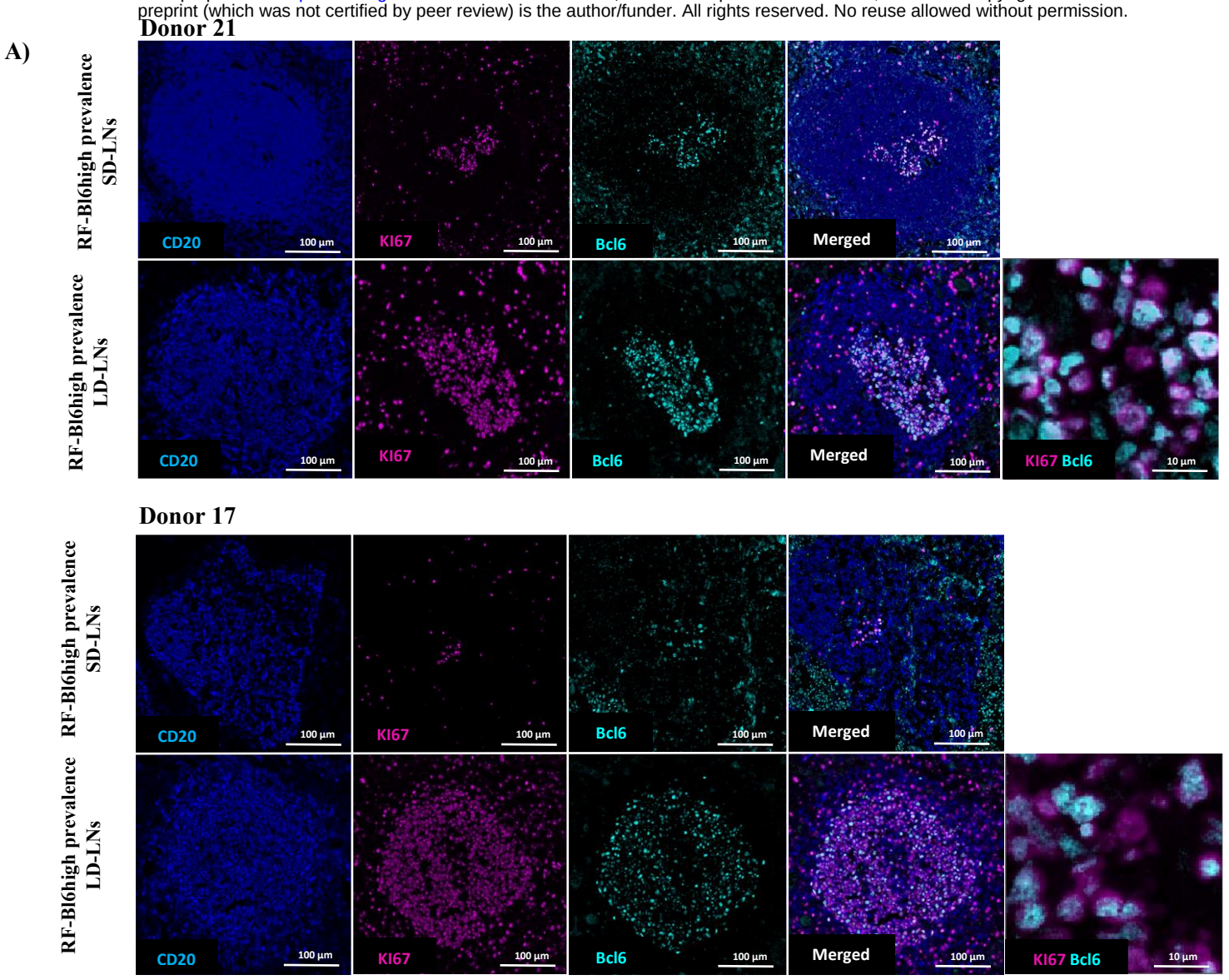

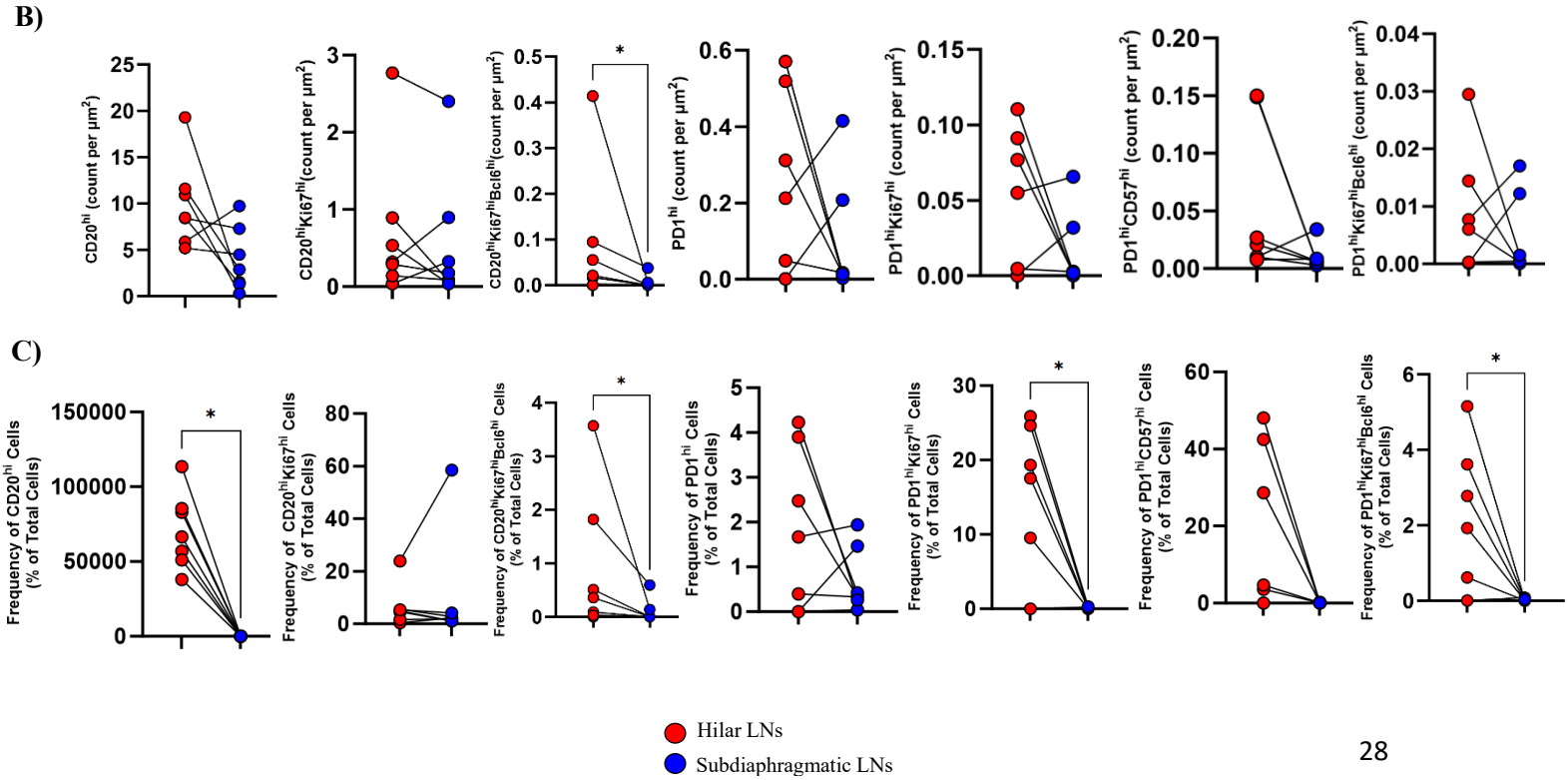

Figure 4

bioRxiv preprint doi: https://doi.org/10.1101/2024.11.07.622471; this version posted November 8, 2024. The copyright holder for this preprint (which was not certified by peer review) is the author/funder. All rights reserved. No reuse allowed without permission.

Figure 4. COVID-19 infection reveals a disconnection in F/GC immunoreactivity between LD-LNs and matched distal subdiaphragmatic LNs. A) Representative fluorescence images (100 µm and 10 µm) showing the $CD20^{high/dim}$, $Ki67^{high}$, and $Bcl6^{high}$ expression in subdiaphragmatic and matched LD-LN follicular areas from two RF-Bcl6high samples (donor 21-upper panel and donor 17-lower panel) ($CD20^{high/dim}$ -blue, $Ki67^{high}$ -magenta, $Bcl6^{high}$ -cyan, and a merged image). **B)** Dot plot graphs showing the cell densities normalized per μm^2 cell counts of B and CD4 T cell subsets in the subdiaphragmatic (blue marks) and matched LD-LNs (red marks). Asterisks denote p-value: * $P \leq 0.05$, ** $P \leq 0.01$, and *** $P \leq 0.001$(Wilcoxon T-Test). **C)** Dot plot graphs showing the cell frequency (%) of total cells of B and CD4 T cell subsets in the subdiaphragmatic (blue marks) and matched LD-LNs (red marks). Asterisks denote p-value: * $P \leq 0.05$, ** $P \leq 0.01$, and *** $P \leq 0.001$(Wilcoxon T-Test).

https://doi.org/10.1101/2024.11.07.622474 ... rsity) posted November 8, 2024. The copyright holder for this
All rights reserved. No reuse allowed without permission.

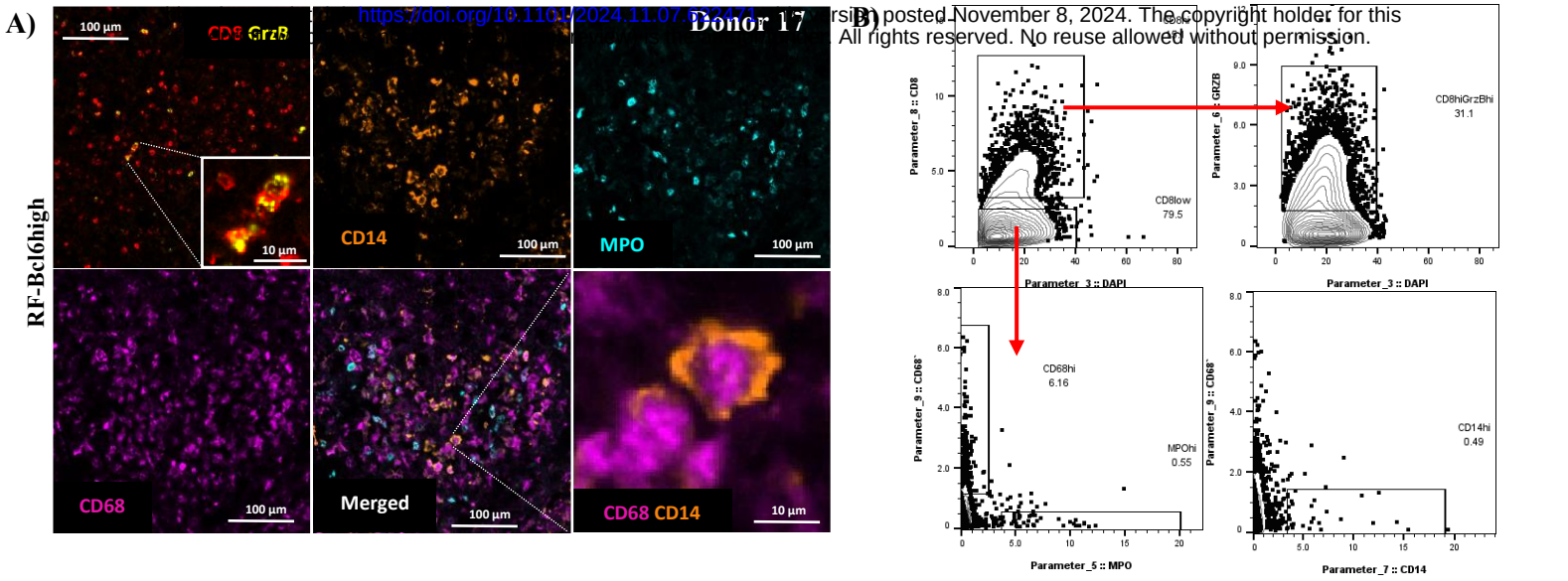

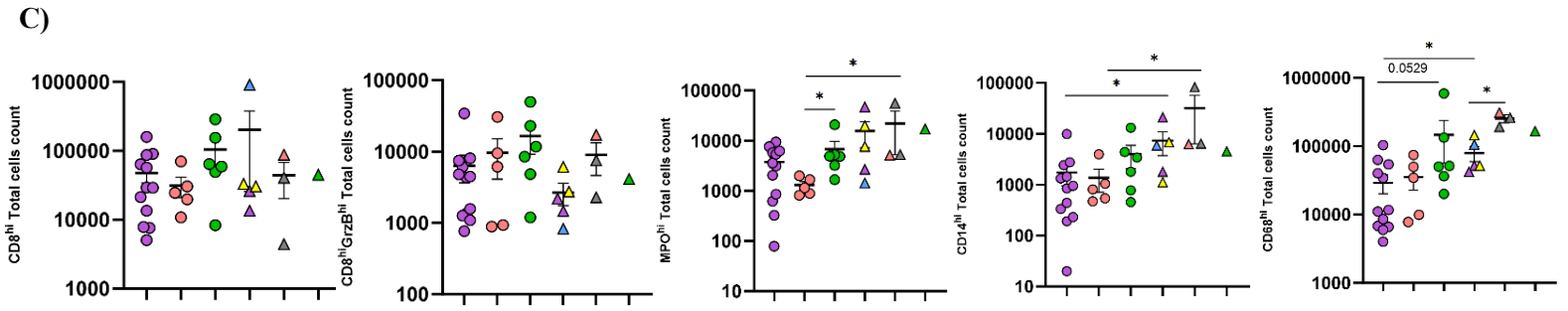

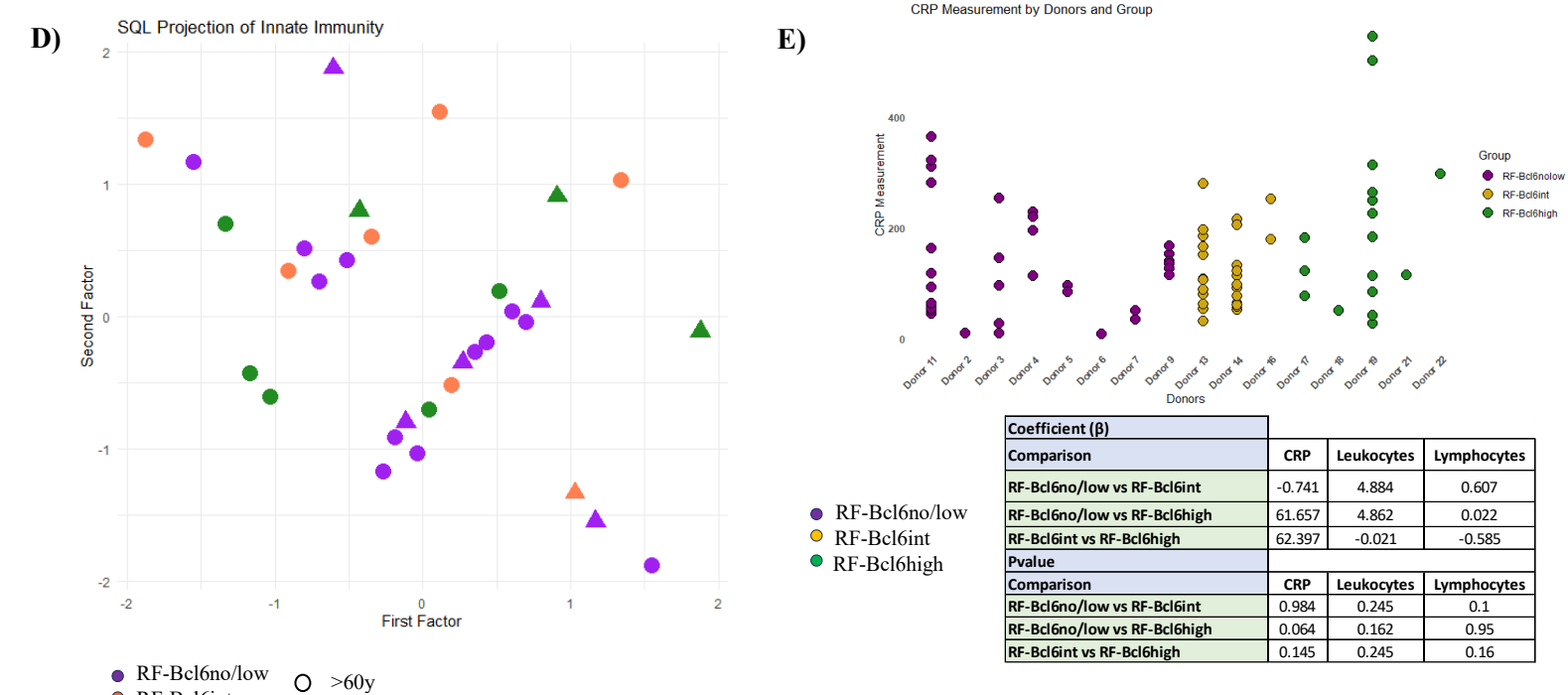

Coefficient (β)			
Comparison	**CRP**	**Leukocytes**	**Lymphocytes**
RF-Bcl6no/low vs RF-Bcl6int	-0.741	4.884	0.607
RF-Bcl6no/low vs RF-Bcl6high	61.657	4.862	0.022
RF-Bcl6int vs RF-Bcl6high	62.397	-0.021	-0.585
Pvalue			
Comparison	**CRP**	**Leukocytes**	**Lymphocytes**
RF-Bcl6no/low vs RF-Bcl6int	0.984	0.245	0.1
RF-Bcl6no/low vs RF-Bcl6high	0.064	0.162	0.95
RF-Bcl6int vs RF-Bcl6high	0.145	0.245	0.16

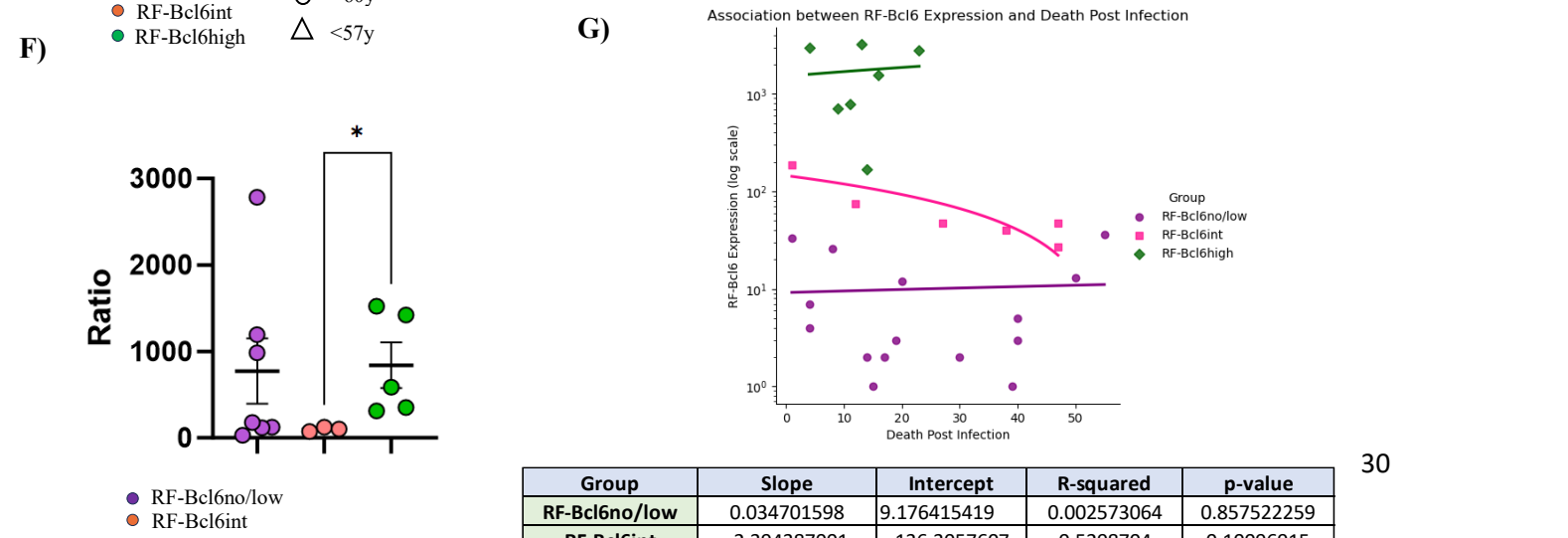

Group	Slope	Intercept	R-squared	p-value
RF-Bcl6no/low	0.034701598	9.176415419	0.002573064	0.857522259
RF-Bcl6int	-2.394387001	136.3057607	0.5298704	0.10096915
RF-Bcl6high	17.41869919	1516.902439	0.006896726	0.859501496

Figure 5

bioRxiv preprint doi: https://doi.org/10.1101/2024.11.07.622471; this version posted November 8, 2024. The copyright holder for this preprint (which was not certified by peer review) is the author/funder. All rights reserved. No reuse allowed without permission.

Figure 5. COVID-19 infection shows no distinct CD8 or innate immunity profile in RF-Bcl6high LD-LNs. A) Representative fluorescence images (100 µm and 10 µm) showing $CD8^{high}$-red, $GrzB^{high}$-yellow, $CD14^{high}$-ceramide, MPO^{high}-cyan, and $CD68^{high}$-magenta expression in a follicular area from RF-Bcl6high tissue (Donor 17). Merged and zoomed areas are also shown. **B)** Gating scheme (Histocytometry) for identifying $CD8^{high}$ T cells and innate immune cell subsets. **C)** Dot plots of total cell counts for $CD8^{high}$, $CD8^{high}GrzB^{high}$, MPO^{high}, $CD14^{high}$, and $CD68^{high}$ cells in the three groups for "Aged" (round) and "Young" (triangle) individuals. Within the "Young" RF-Bcl6no/low group, the blue triangle represents an axillary lymph node (donor 25), and yellow triangles represent para-aortic and mediastinal lymph nodes from donor 29. Within the "Young" RF-Bcl6int group, two different Mediastinal lymph nodes from the same donor (donor 24-a and donor 24-b) are depicted by the grey triangles. Asterisks denote p-values: * $P \leq 0.05$, ** $P \leq 0.01$, *** $P \leq 0.001$ (Mann-Whitney T-Test). **D)** SQL clustering projection of $CD8^{high}$ T cells and innate immune cell subsets based on $CD14^{high}$, $CD68^{high}$, MPO^{high}, $CD8^{high}$, and $CD8^{high}GrzB^{high}$ counts cell counts in the three groups (RF-Bcl6no/low in purple, RF-Bcl6int in pink and, RF-Bcl6high in green), for the "Aged" (round marks) and "Young" (triangle marks). **E)** Dot plots showing CRP (mg/L) over time in "Aged" individuals from the three subgroups. Statistical analysis via Mixed Linear Regression, with summary in the lower panel. **F)** Ratio of LD-LNs MPO to circulating granulocytes (neutrophils, basophils, eosinophils) in the three subgroups. Asterisks denote p-values: * $P \leq 0.05$, ** $P \leq 0.01$, *** $P \leq 0.001$ (Mann-Whitney T-Test). **G)** Scatter plot with regression lines showing the association between RF-Bcl6 expression and death post-infection (DPI) across the three subgroups. RF-Bcl6 expression is on a logarithmic scale on the y-axis, and DPI on the x-axis. Data points: purple circles (RF-Bcl6no/low), pink squares (RF-Bcl6int), and green diamonds (RF-Bcl6high). Trend lines and a table summarizing key statistical parameters (slope, intercept, R-squared, p-value) are shown in the lower panel.

bioRxiv preprint doi: https://doi.org/10.1101/2024.11.07.622471; this version posted November 8, 2024. The copyright holder for this preprint (which was not certified by peer review) is the author/funder. All rights reserved. No reuse allowed without permission.

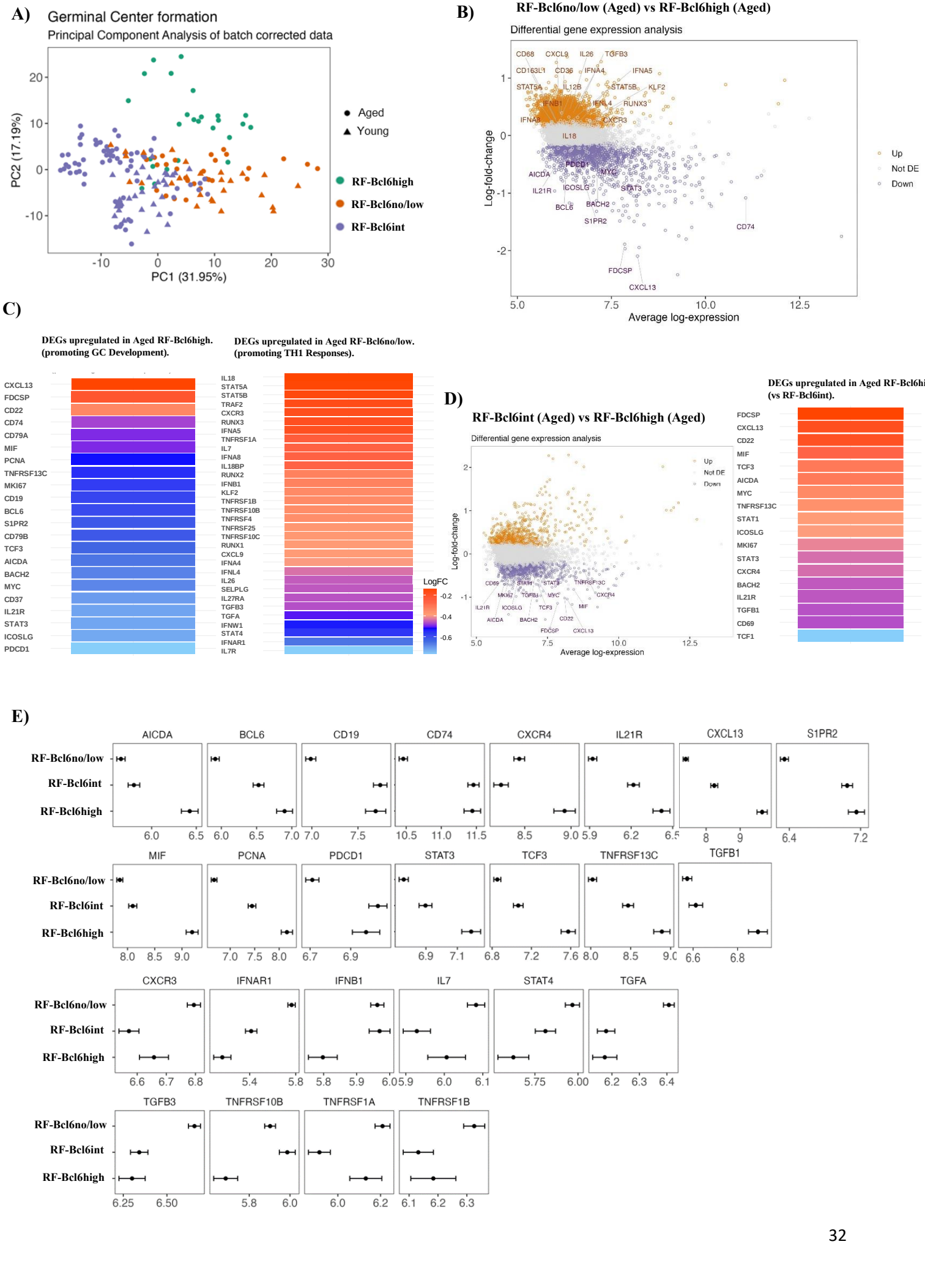

Figure 6

bioRxiv preprint doi: https://doi.org/10.1101/2024.11.07.622471; this version posted November 8, 2024. The copyright holder for this preprint (which was not certified by peer review) is the author/funder. All rights reserved. No reuse allowed without permission.

Figure 6. Distinct *in situ* transcriptomic profiles are associated with RF-Bcl6high follicles in LD-LNs. A) Principal component analysis (PCA) based on the 2 first components PC1 (31.95%) and PC2 (17.19%) of the gene expression after normalization and batch correction in the three groups, RF-Bcl6high (green dots), RF-Bcl6int (orange dots), and RF-Bcl6no/low (purple dots), for the "Aged" (round marks) and "Young" (triangle marks) individuals. **B)** Volcano plot showing differentially expressed genes in RF-Bcl6no/low vs RF-Bcl6high individuals from the "Aged" group. Orange dots present genes significantly increased in the RF-Bcl6no/low group and purple dots genes significantly increased in the RF-Bcl6high group. **C)** Heatmaps of differentially expressed genes (DEGs) promoting "GC development" upregulated in the RF-Bcl6high group (left image) or promoting "TH1 responses" upregulated in the RF-Bcl6no/low "Aged" group (right image). **D)** Volcano plot for DEGs between RF-Bcl6int and RF-Bcl6high individuals from the "Aged" group. Orange dots show genes significantly increased in the RF-Bcl6int group; while purple dots show genes significantly increased in the RF-Bcl6high of the "Aged" group. Heatmap of DEGs in RF-Bcl6high "Aged" individuals. **E)** Expression levels (log-transformed expression, x-axis) of specific genes across three RF-Bcl6 expression groups (y-axis).

bioRxiv preprint doi: https://doi.org/10.1101/2024.11.07.622471; this version posted November 8, 2024. The copyright holder for this preprint (which was not certified by peer review) is the author/funder. All rights reserved. No reuse allowed without permission.

A)

Reactome RF-Bcl6no/low (Aged) vs RF-Bcl6no/low (Aged)

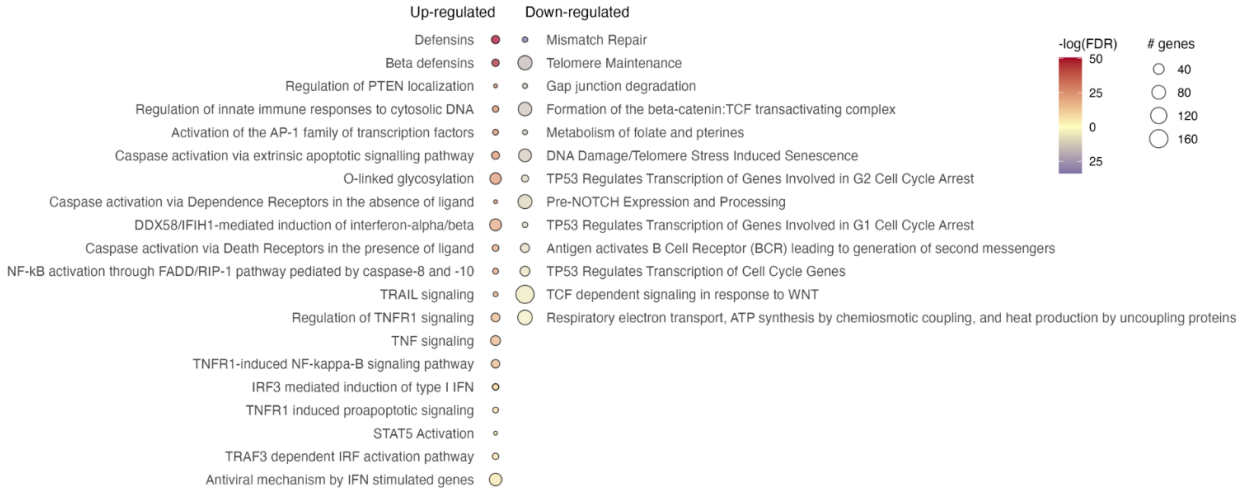

B)

RF-Bcl6no/low (Young) vs RF-Bcl6no/low (Aged)

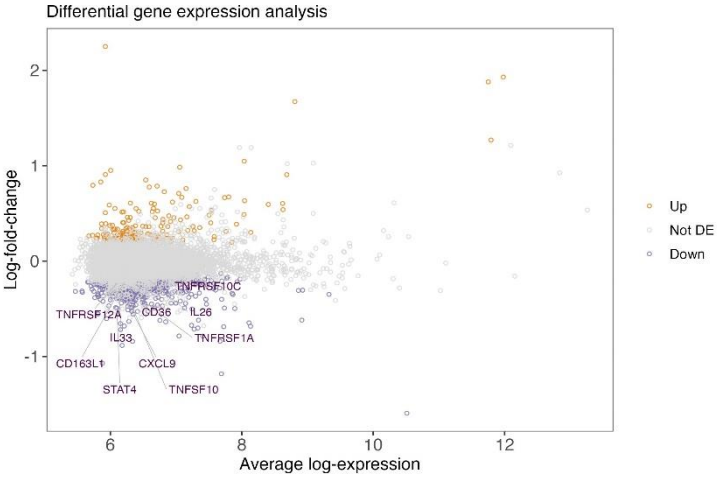

TNF-Family Gene Members Upregulated in Aged RF-Bcl6no/low. (vs Young RF-Bcl6no/low)

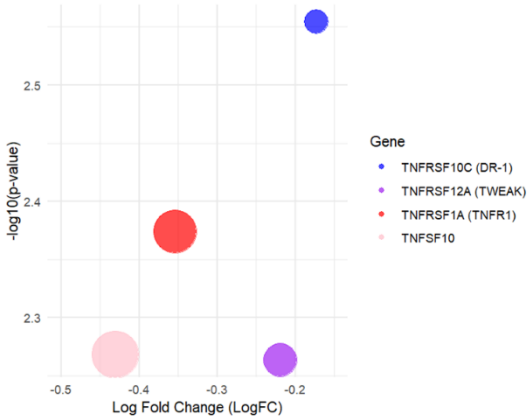

TNF-Family Pathway Members Upregulated in Aged RF-Bcl6no/low. (vs Young RF-Bcl6no/low)

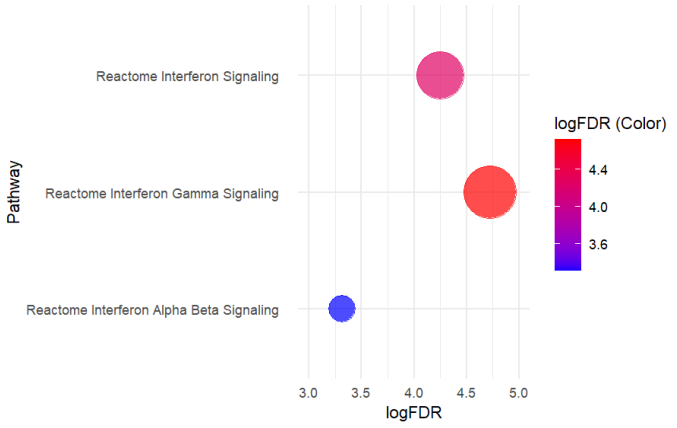

C)

RF-Bcl6int (Young) vs RF-Bcl6int (Aged)

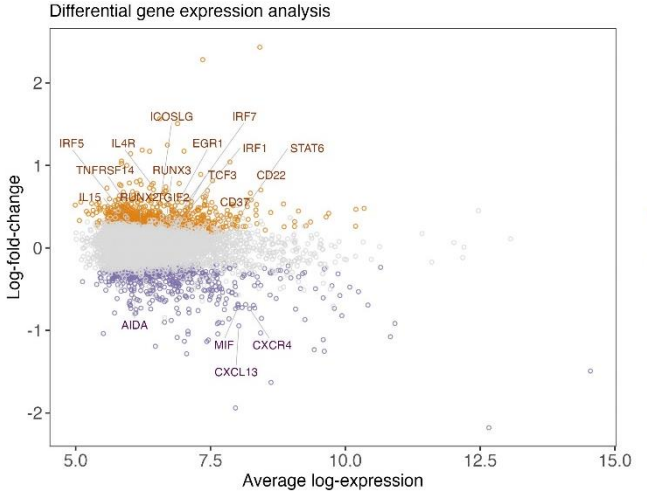

DEGs upregulated in Young RF-Bcl6int. (vs Aged RF-Bcl6int)

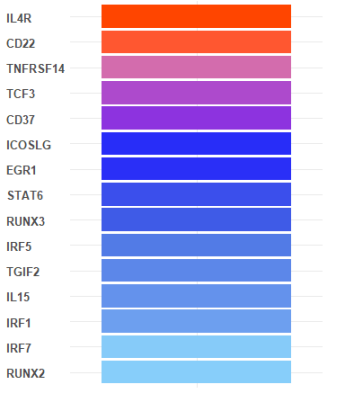

DEGs upregulated in Aged RF-Bcl6int. (vs Young RF-Bcl6int)

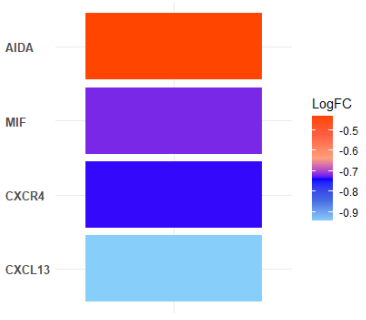

Figure 7

bioRxiv preprint doi: https://doi.org/10.1101/2024.11.07.622471; this version posted November 8, 2024. The copyright holder for this preprint (which was not certified by peer review) is the author/funder. All rights reserved. No reuse allowed without permission.

Figure 7. Altered follicular/GC transcriptomic profiling in LDLNs with respect to age. A) Dot plot of Reactome pathways significantly enriched in RF-Bcl6no/low vs RF-Bcl6high "Aged" individuals. The dot size represents the number of differentially expressed genes upregulated (left column) or downregulated (right column) in the RF-Bcl6no/low compared to RF-Bcl6high individuals. The color dots show the -log (FDR) representing the negative logarithm of the False Discovery Rate. **B)** Volcano plot for DEGs in RF-Bcl6no/low individuals from the "Young" and "Aged" subgroups. Orange dots show genes significantly increased in the "Young" RF-Bcl6no/low tissues and purple dots show genes significantly increased in the "Aged" RF-Bcl6no/low tissues. The bottom left panel displays a dot plot of TNF-family genes showing Log Fold Change (LogFC) and statistical significance (-log10(P-value)) in the "Aged" RF-Bcl6no/low group compared to the "Young" RF-Bcl6no/low group, with larger dots indicating higher significance and colors differentiating the genes. The bottom right panel features a bubble plot demonstrating the upregulation of "TNF-family-related" pathways, where the bubble size and position represent the degree of pathway activation and the color signifies FDR-adjusted significance levels.**C)** Volcano for DEGs in RF-Bcl6int individuals from the "Young" and "Aged" subgroups. The volcano plot is depicted with the log-fold change of each gene and the average log expression of each gene. Orange dots show genes highly expressed in "Young" RF-Bcl6int tissues and purple dots show genes highly expressed in "Aged" RF-Bcl6int tissues. Heatmap plots of DEGs highly expressed in the "Young" (left image) and the "Aged" (right image) RF-Bcl6int subgroup.

bioRxiv preprint doi: https://doi.org/10.1101/2024.11.07.622471; this version posted November 8, 2024. The copyright holder for this preprint (which was not certified by peer review) is the author/funder. All rights reserved. No reuse allowed without permission.

A)

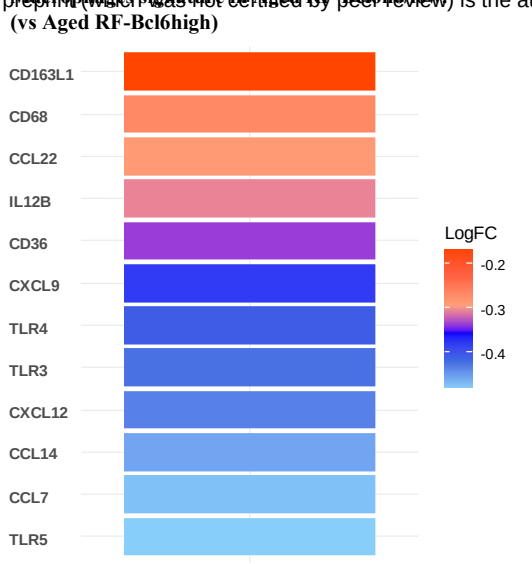

B)

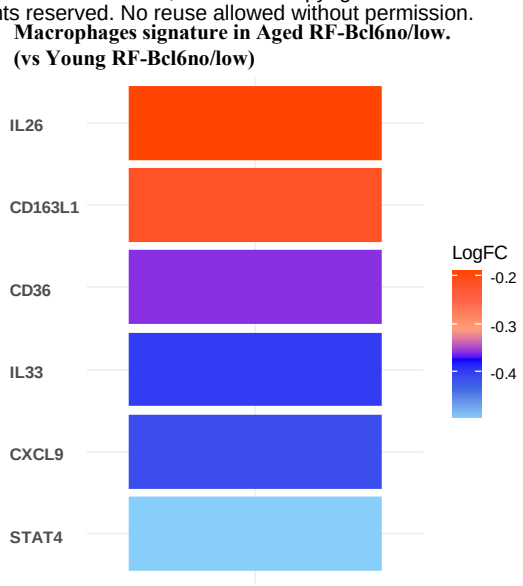

C)

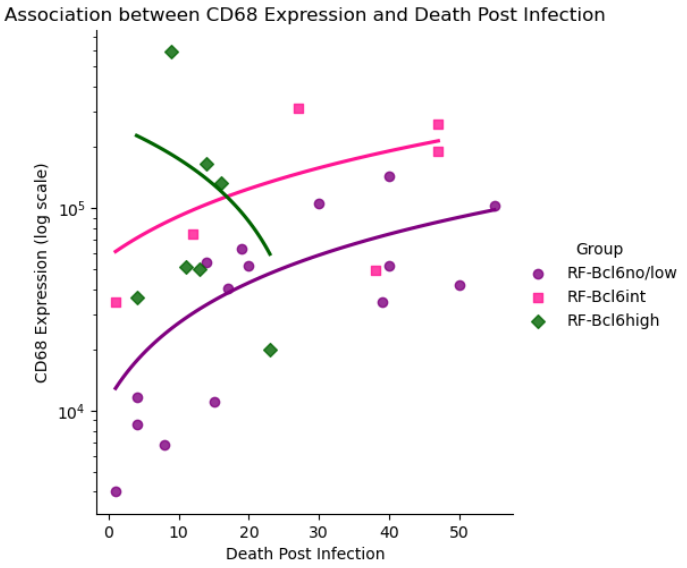

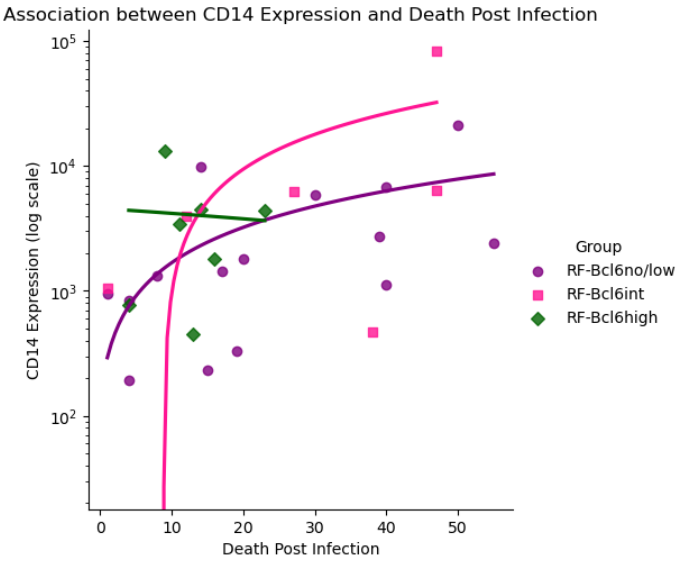

CD68 vs DPI

Group	Slope	Intercept	R-squared	p-value
RF-Bcl6no/low	1580.43885	11363.25129	0.440497014	0.006978273
RF-Bcl6int	3347.091396	57855.37999	0.29279925	0.267554279
RF-Bcl6high	-8897.519648	264121.1098	0.068388864	0.571066199

CD14 vs DPI

Group	Slope	Intercept	R-squared	p-value
RF-Bcl6no/low	154.4762081	137.6979711	0.236448777	0.066763956
RF-Bcl6int	847.5672083	-7515.75997	0.248047324	0.314703937
RF-Bcl6high	-39.9898374	4578.012195	0.003019513	0.906854591

Figure 8

bioRxiv preprint doi: https://doi.org/10.1101/2024.11.07.622471; this version posted November 8, 2024. The copyright holder for this preprint (which was not certified by peer review) is the author/funder. All rights reserved. No reuse allowed without permission.

Figure 8. "Aged" RF-Bcl6no/low follicles exhibit a distinct *in situ* macrophage profile in COVID-19 LD-LNs. A) Heatmap illustrating macrophage-specific gene expression DEGs in RF-Bcl6no/low compared to RF-Bcl6high in LD-LNs from "Aged" COVID-19 infected individuals. **B)** Heatmap illustrating macrophage-specific gene expression DEGs in "Aged" compared to "Young" RF-Bcl6no/low in LD-LNs COVID-19 infected individuals. **C)** Linear regression analysis showing the association between the cell densities of CD68 and death post-infection (DPI) (left panel) or CD14 and DPI (right panel) in LD-LNs from "Aged" COVID-19-infected individuals. CD68 and CD14 cell densities are on a logarithmic scale on the y-axis, and DPI on the x-axis. Data points: purple circles (RF-Bcl6no/low), pink squares (RF-Bcl6int), and green diamonds (RF-Bcl6high). A table summarizing key statistical parameters for each group, including the slope, intercept, R-squared, and p-value based on the linear regression analysis is shown too (lower panel).

bioRxiv preprint doi: https://doi.org/10.1101/2024.11.07.622471; this version posted November 8, 2024. The copyright holder for this preprint (which was not certified by peer review) is the author/funder. All rights reserved. No reuse allowed without permission.

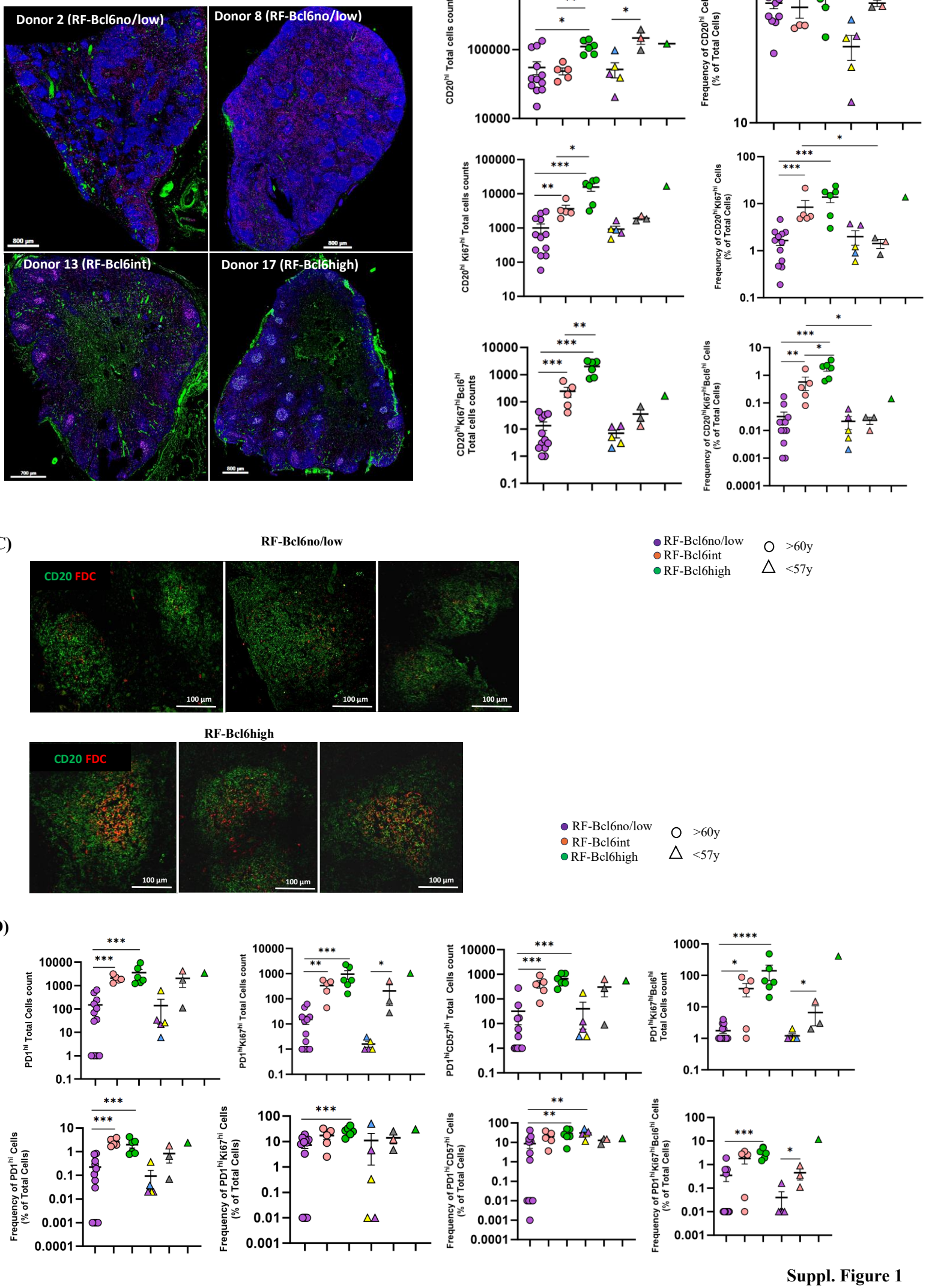

Suppl. Figure 1

bioRxiv preprint doi: https://doi.org/10.1101/2024.11.07.622471; this version posted November 8, 2024. The copyright holder for this preprint (which was not certified by peer review) is the author/funder. All rights reserved. No reuse allowed without permission.

Suppl. Figure 1. A) Representative fluorescence images showing tissues (overview) from each group in a RF-Bcl6no/low tissue (Donor 2 and Donor 8), RF-Bcl6int (Donor 13), and RF-Bcl6high (Donor 17). **B)** Dot plot graphs showing the total cell counts and frequency (%) of total cells of B cell subsets ($CD20^{high/dim}$, $CD20^{high/dim}Ki67^{high}$, and $CD20^{high/dim}Ki6^{high}Bcl6^{high}$) in the three groups for the "Aged" (round marks) and "Young" (triangle marks) individuals. Within the "Young" RF-Bcl6no/low group, the blue triangle represents an axillary lymph node (donor 25), and the yellow triangles represent para-aortic and mediastinal lymph nodes from donor 29. Within the "Young" RF-Bcl6int group, two different Mediastinal lymph nodes from the same donor (donor 24-a and donor 24-b) are depicted by the grey triangles. Asterisks denote p-values: * $P \leq 0.05$, ** $P \leq 0.01$, *** $P \leq 0.001$ (Mann-Whitney T-Test). **C)** Representative fluorescence images (100 µm) showing the expression of FDC (red) in follicular areas (CD20, green) from RF-Bcl6no/low (n=3) and RF-Bcl6high (n=3) tissues. **D)** Dot plot graphs showing the total cell counts and frequency (%) of total cells, of T cell subsets ($PD1^{high}$, $PD1^{high}Ki67^{high}$, $PD1^{high}CD57^{high}$, and $PD1^{high}Ki67^{high}Bcl6^{high}$) in the three groups for the "Aged" (round marks) and "Young" (triangle marks) individuals. Within the "Young" RF-Bcl6no/low group, the blue triangle represents an axillary lymph node (donor 25), and the yellow triangles represent para-aortic and mediastinal lymph nodes from donor 29. Within the "Young" RF-Bcl6int group, two different Mediastinal lymph nodes from the same donor (donor 24-a and donor 24-b) are depicted by the grey triangles. Asterisks denote p-values: * $P \leq 0.05$, ** $P \leq 0.01$, *** $P \leq 0.001$ (Mann-Whitney T-Test).

bioRxiv preprint doi: https://doi.org/10.1101/2024.11.07.622471; this version posted November 8, 2024. The copyright holder for this preprint (which was not certified by peer review) is the author/funder. All rights reserved. No reuse allowed without permission.

A)

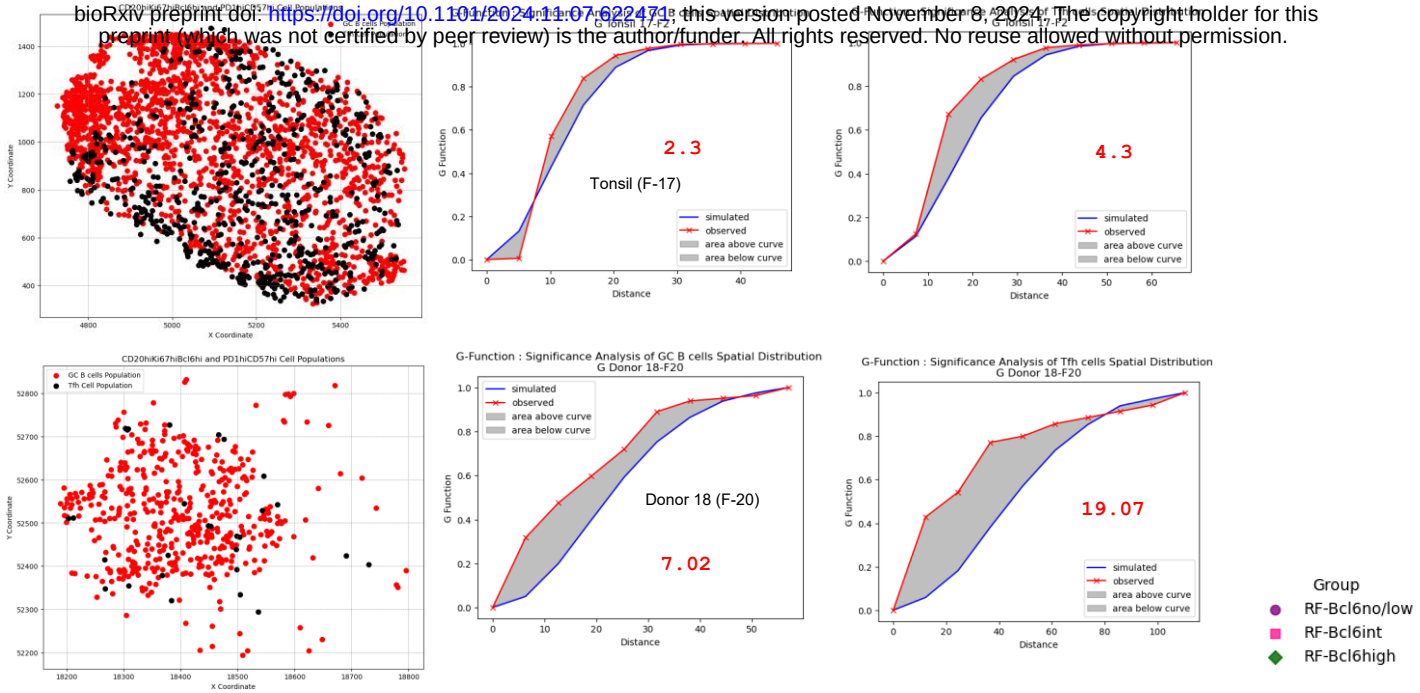

B)

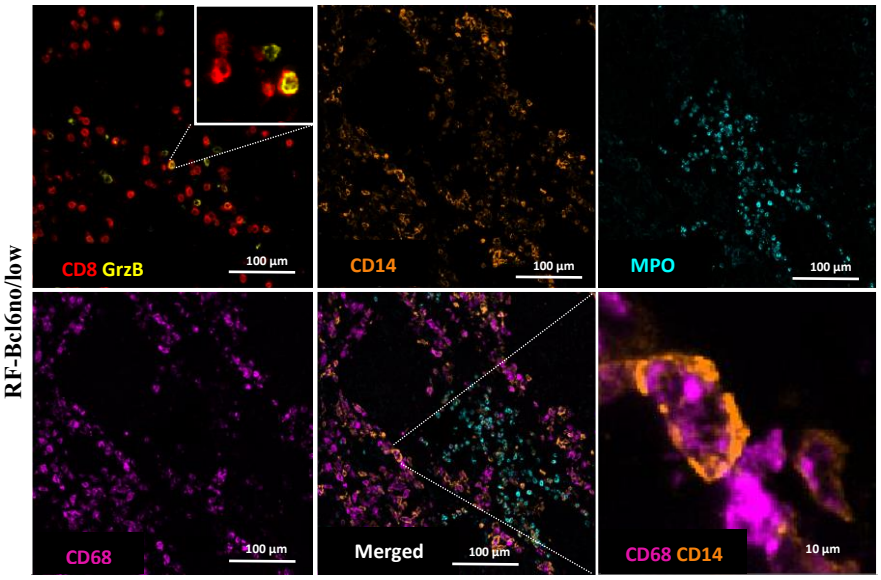

D)

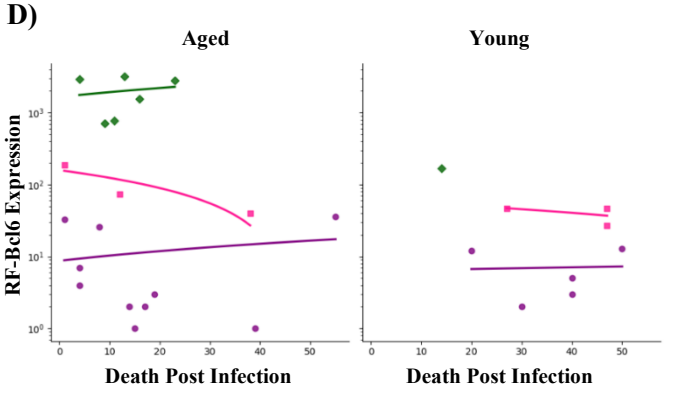

Age	Group	Slope	Intercept	R-squared	p-value
Aged	RF-Bcl6no/low	0.158232686	8.715104724	0.035944215	0.599861061
Aged	RF-Bcl6int	-3.470914127	159.0055402	0.7452116	0.336842153
AGed	RF-Bcl6high	27.57006369	1653.94586	0.02491451	0.765201305
Young	RF-Bcl6no/low	0.019230769	6.307692308	0.001814	0.945784416
Young	RF-Bcl6int	-0.5	60.5	0.25	0.666666667
Young	RF-Bcl6high	nan	nan	nan	nan

C)

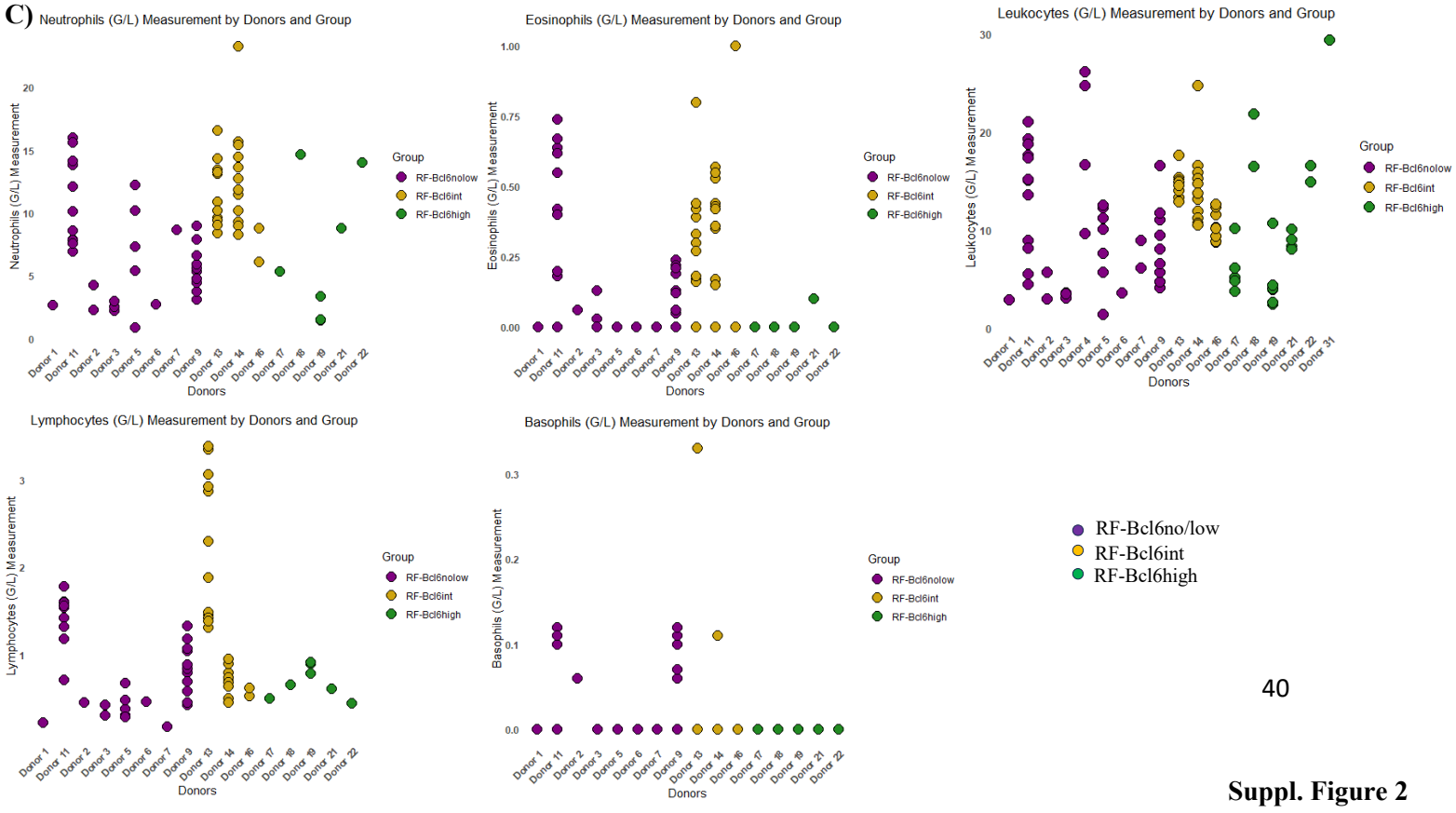

Suppl. Figure 2

bioRxiv preprint doi: https://doi.org/10.1101/2024.11.07.622471; this version posted November 8, 2024. The copyright holder for this preprint (which was not certified by peer review) is the author/funder. All rights reserved. No reuse allowed without permission.

Suppl. Figure 2. A) Point pattern distribution graphs showing a follicular area in control tonsillar tissue (top, Tonsil 17 – F2) and in a RF-Bcl6high tissue (bottom, Donor 18 – F20) ($CD20^{high/dim}Ki67^{high}Bcl6^{high}$-red and $PD1^{high}CD57^{high}$- black) and their corresponding graphic representation of the G-Function analysis showing the proximity of the G curve (red curve) to the theoretical estimate curve (Poisson curve, blue curve). The shade gray area represents the area between the two curves measured. **B)** Representative fluorescence image (100µm) showing a follicular area in a RF-Bcl6no/low tissue (Donor 2); $CD8^{high}$-red and $GrzB^{high}$-yellow (insert: a zoomed area is shown, 10µm), $CD14^{high}$-orange, MPO^{high}-cyan, $CD68^{high}$-magenta as well as a merged image are shown. The zoomed image shows the localization of $CD68^{high}$-magenta and $CD14^{high}$-orange. **C)** Dot plots showing serological measurement for total Neutrophils (G/L), Eosinophils (G/L), Leukocytes (G/L), Lymphocytes (G/L) and Basophils (G/L) at different time points in the group of "Aged" individuals for RF- Bcl6no/low (purple dots), RF-Bcl6int (yellow dots) and RF-Bcl6high (green dots). **D)** Scatter plot with regression lines illustrating the association between RF-Bcl6 expression and death post-infection (DPI) across the three subgroups from "Aged" (left panel) and "Young" (right panel). RF-Bcl6 expressions are plotted on a logarithmic scale on the y-axis, while DPI is shown on the x-axis. Data points for the RF-Bcl6no/low group are represented by purple circles, for the RF-Bcl6int group by pink squares, and for the RF-Bcl6high group by green diamonds. Summary table of the Mixed Linear Regression Model performed to compare RF-Bcl6no/low (reference) vs RF-Bcl6int, RF-Bcl6no/low (reference) vs RF-Bcl6high, and RF-Bcl6int (reference) vs RF-Bcl6high from the "Aged" group for the measurement of CRP. The results, including p-values and intercept (β) values, are summarized in the table. The intercept (β) represents the average outcome value for the reference group when all other predictors are zero. A p-value less than 0.05 indicates a statistically significant difference between the groups. Statistical analysis has been conducted using a Mixed Linear Regression model.

bioRxiv preprint doi: https://doi.org/10.1101/2024.11.07.622471; this version posted November 8, 2024. The copyright holder for this preprint (which was not certified by peer review) is the author/funder. All rights reserved. No reuse allowed without permission.

A)

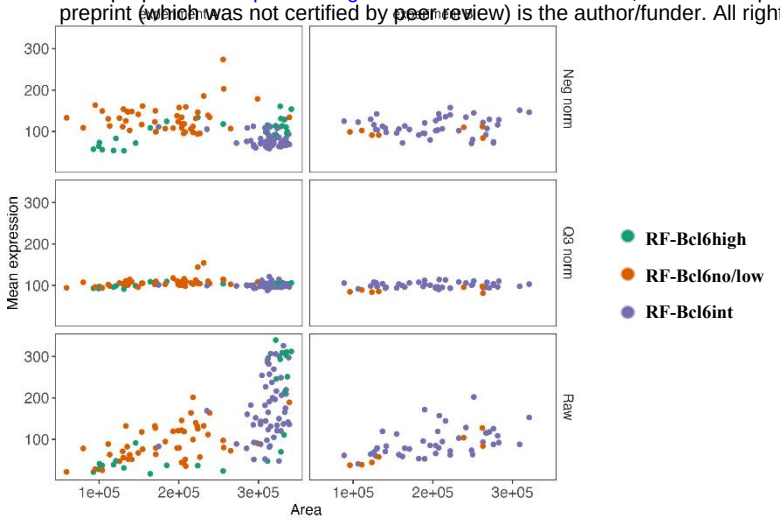

B)

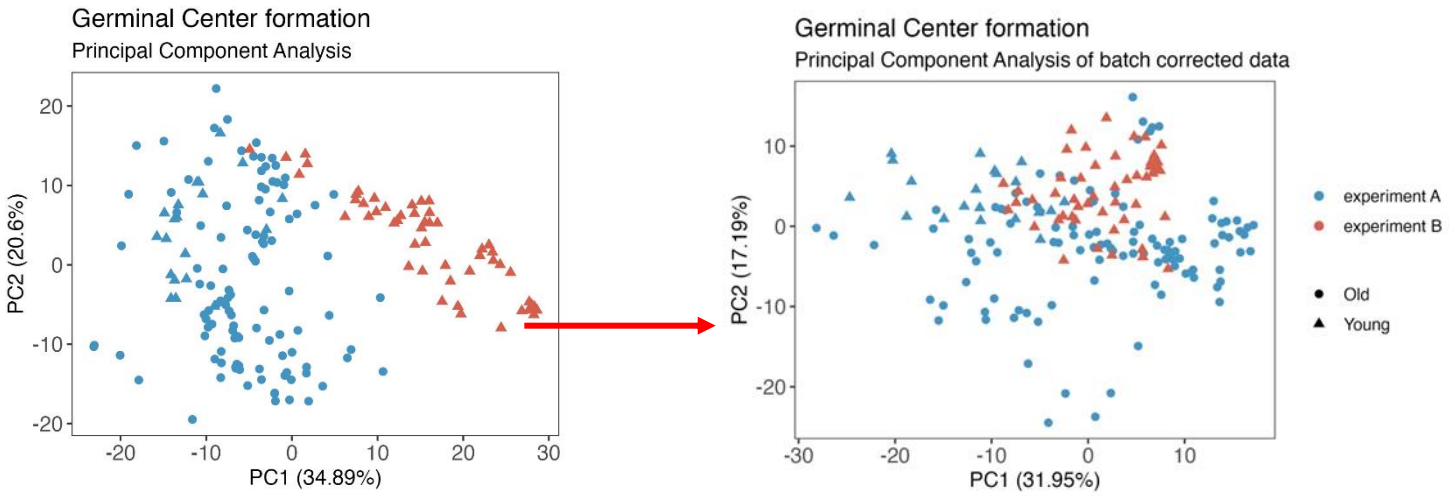

C)

RF-Bcl6high ("Aged") (Donor 18) / GC promoting gene-set.

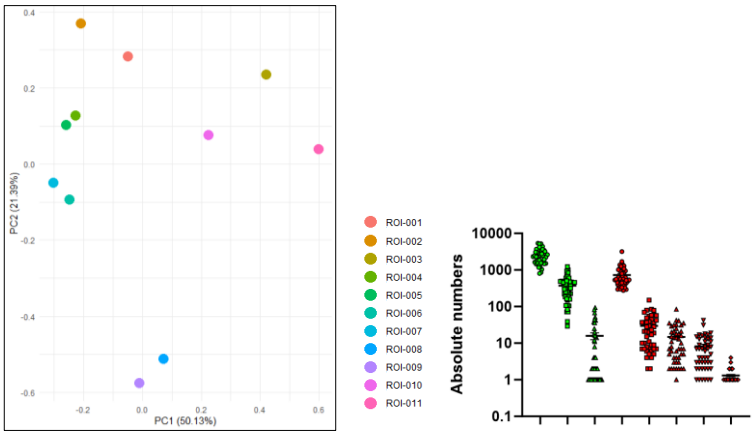

RF-Bcl6high ("Aged") (Donor 17) / GC promoting gene-set.

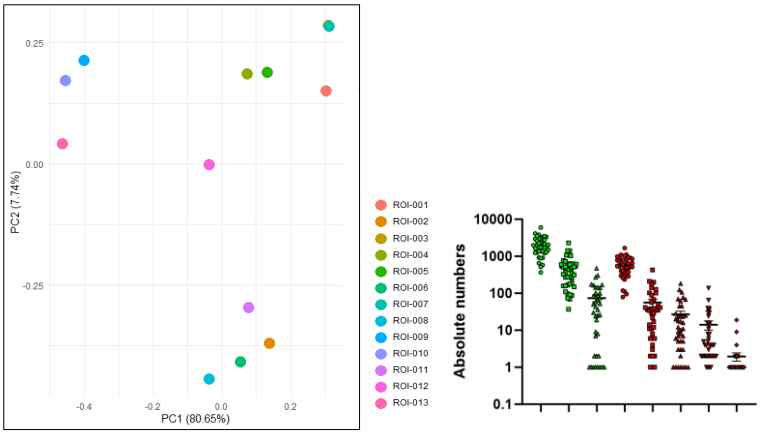

RF-Bcl6high ("Aged") (Donor 19) / GC promoting gene-set.

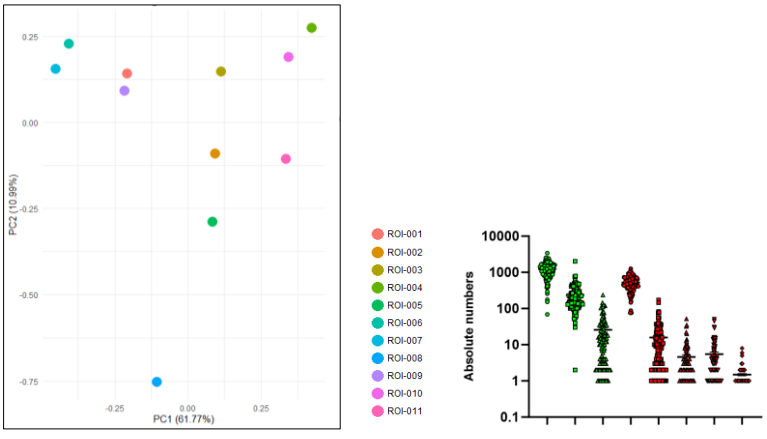

$CD20^{hi/dim}$
$CD20^{hi/dim}$ $Ki67^{hi}$
$CD20^{hi/dim}$ $Ki67^{hi}$ $Bcl6^{hi}$

$PD1^{hi}$
$PD1^{hi}$ $CD57^{hi}$
$PD1^{hi}$ $Ki67^{hi}$
$PD1^{hi}$ $Ki67^{hi}$ $Bcl6^{hi}$

Suppl. Figure 3

bioRxiv preprint doi: https://doi.org/10.1101/2024.11.07.622471; this version posted November 8, 2024. The copyright holder for this preprint (which was not certified by peer review) is the author/funder. All rights reserved. No reuse allowed without permission.

Suppl. Figure 3. A) Visualizing plots of the normalized GeoMx-generated data per ROI. The figure represents a series of scatter plots comparing the mean expression levels across different ROIs for two experiments (A and B) under three different normalization conditions: Negative normalization (Neg norm), Q3 normalization (Q3 norm), and Raw data (Raw). The data points are color-coded to represent the three different groups: RF-Bcl6high (green), RF-Bcl6int (orange) and RF-Bcl6no/low (purple). **B)** Principal Component Analysis (PCA) plots before and after batch correction. The first plot illustrates the PCA before batch correction (left image), with data from Experiment A (cyan) and Experiment B (red) showing clear separation along PC1 (34.89%) and PC2 (20.6%), indicating batch effect. The second plot (right image), after batch correction using the Trimmed Mean of M-values (TMM) normalization and RUV-4 correction, displays data from Experiment A (cyan) and Experiment B (red) along PC1 (31.95%) and PC2 (17.19%). **C)** PCA plots showing the distribution of the follicular areas (ROIs), based on the expression of the gene set favoring GC-development, in RF-Bcl6high subgroup (Donor 18, Donor 17, Donor 19). The plots were generated using RStudio based on genes expression extracted from the GeoMx. The absolute numbers of B ($CD20^{high/dim}$, $CD20^{high/dim}Ki67^{high}$, and $CD20^{high/dim}Ki67^{high}Bcl6^{high}$) and TFH ($PD1^{high}$, $PD1^{high}CD57^{high}$, $PD1^{high}Ki67^{high}$, $PD1^{high}Ki67^{high}Bcl6^{high}$) subsets in individual follicles from the same individuals are shown too.

bioRxiv preprint doi: https://doi.org/10.1101/2024.11.07.622471; this version posted November 8, 2024. The copyright holder for this preprint (which was not certified by peer review) is the author/funder. All rights reserved. No reuse allowed without permission.

A)

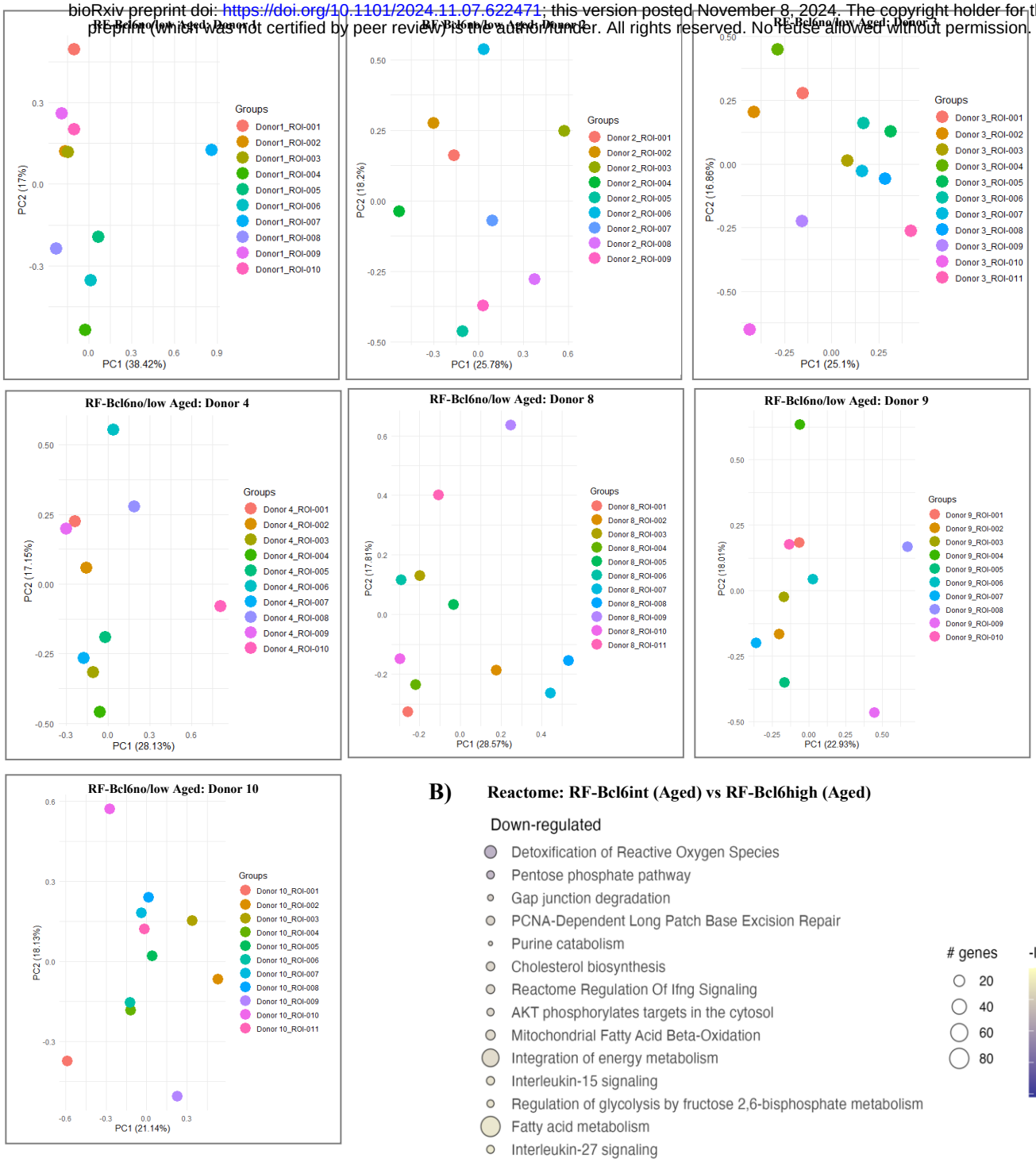

B) **Reactome: RF-Bcl6int (Aged) vs RF-Bcl6high (Aged)**

C) **Comparison between two LDLNs (24-a/24-b) from the same donor.**

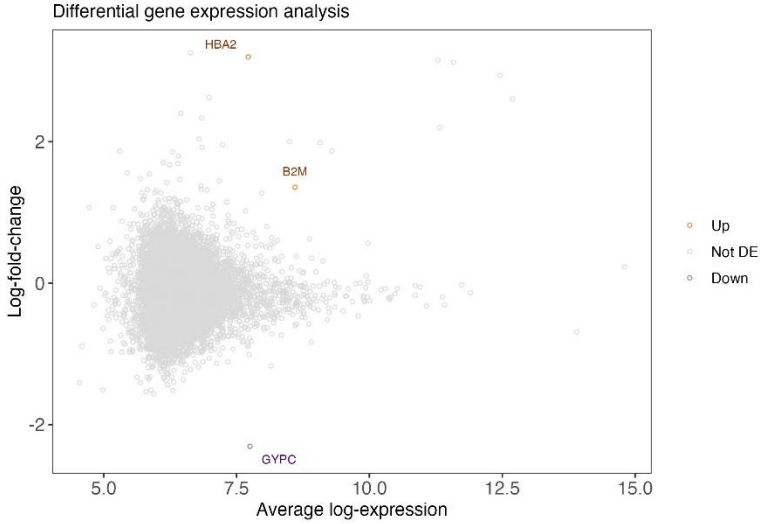

D) **Comparison between distal (Axillary) and LDLNs (RF-Bcl6no/low young group).**

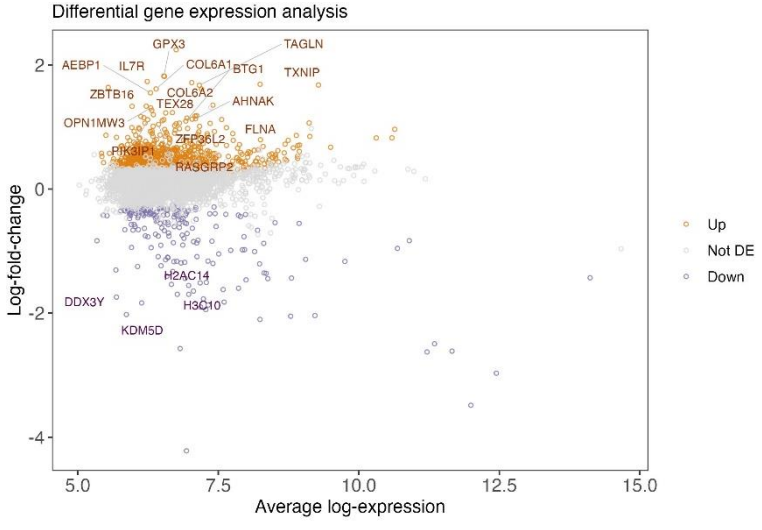

Suppl. Figure 4

bioRxiv preprint doi: https://doi.org/10.1101/2024.11.07.622471; this version posted November 8, 2024. The copyright holder for this preprint (which was not certified by peer review) is the author/funder. All rights reserved. No reuse allowed without permission.

Suppl. Figure 4. A) PCA plots showing the distribution of follicular areas (ROIs), based on the expression of the gene set favoring TH1 responses, in the RF-Bcl6no/low group (Donor 1, Donor 2, Donor 3, Donor 4, Donor 8, Donor 9, Donor 10). The plots were generated using RStudio based on genes expression extracted from the GeoMx. **B)** Reactome pathways analysis showing pathways upregulated in "Aged" RF-Bcl6high compared to "Aged" RF-Bcl6int (downregulated). **C)** Volcano plot of gene expression for two RF-Bcl6no/low LD-LNs (24-a and 24-b) from the same donor (Donor 24). **D)** Volcano plot of gene expression between distal (Axillary, Donor 25) RF-Bcl6no/low and LD-LNs RF-Bcl6no/low from the "Young" group. Volcano plot is depicted with the log-fold change of each gene and the average log expression of each gene. Orange dots show genes significantly increased in the Axillary LN and purple dots genes significantly increased in the LD-LNs from the same RF-Bcl6no/low "Young" group.

bioRxiv preprint doi: https://doi.org/10.1101/2024.11.07.622471; this version posted November 8, 2024. The copyright holder for this preprint (which was not certified by peer review) is the author/funder. All rights reserved. No reuse allowed without permission.

Table 1. Study Cohort. The origin, anatomical location, demographic data, and the assay applied for each tissue and donor are listed.

	Donor	Origin	Lymph Nodes Location	Gender	Age (Years)	Analysis
Aged RF-Bcl6no/low	Donor 1	Switzerland	Hilar	F	73	Imaging/GeoMx
	Donor 2	Switzerland	Hilar	M	96	Imaging/GeoMx
	Donor 3	Switzerland	Subdiaphragmatic/Hilar	M	72	Imaging/GeoMx
	Donor 4	Switzerland	Hilar	M	86	Imaging/GeoMx
	Donor 5	Switzerland	Hilar	F	76	Imaging
	Donor 6	Switzerland	Hilar	F	63	Imaging
	Donor 7	Switzerland	Hilar	F	73	GeoMx
	Donor 8	Switzerland	Hilar	M	61	Imaging/GeoMx
	Donor 9	Switzerland	Subdiaphragmatic/Hilar	F	73	Imaging/GeoMx
	Donor 10	Switzerland	Hilar	M	61	Imaging/GeoMx
	Donor 11	Switzerland	Subdiaphragmatic/Hilar	F	76	Imaging
	Donor 26	Chicago	Para-esophageal	F	60	Imaging/GeoMx
	Donor 27	Chicago	Para-aortic	F	61	Imaging/GeoMx
Aged RF-Bcl6int	Donor 12	Switzerland	Hilar	M	79	Imaging/GeoMx
	Donor 13	Switzerland	Hilar	M	69	Imaging/GeoMx
	Donor 14	Switzerland	Subdiaphragmatic/Hilar	M	74	Imaging
	Donor 15	Switzerland	Subdiaphragmatic/Hilar	M	86	Imaging
	Donor 16	Switzerland	Hilar	M	89	Imaging/GeoMx
Aged RF-Bcl6high	Donor 17	Switzerland	Subdiaphragmatic/Hilar	M	87	Imaging/GeoMx
	Donor 18	Switzerland	Hilar	F	74	Imaging/GeoMx
	Donor 19	Switzerland	Hilar	M	75	Imaging/GeoMx
	Donor 20	Switzerland	Hilar	M	64	Imaging
	Donor 21	Switzerland	Subdiaphragmatic/Hilar	M	65	Imaging
	Donor 22	Switzerland	Hilar	F	71	Imaging
Young RF-Bcl6no/low	Donor 23	Chicago	Para-tracheal	M	57	Imaging/GeoMx
	Donor 24-a / Donor 24-b	Chicago	Mediastinal	M	36	Imaging/GeoMx
	Donor 25	Chicago	Axillary	F	50	Imaging/GeoMx
	Donor 28	Chicago	Mediastinal	F	35	Imaging/GeoMx
Young RF-Bcl6int	Donor 29-a	Chicago	Mediastinal	M	46	Imaging/GeoMx
	Donor 29-b	Chicago	Para-aortic	M	46	Imaging/GeoMx
	Donor 30	Chicago	Mediastinal	M	54	Imaging/GeoMx
Young RF-Bcl6high	Donor 31	Switzerland	Hilar	M	36	Imaging

bioRxiv preprint doi: https://doi.org/10.1101/2024.11.07.622471; this version posted November 8, 2024. The copyright holder for this preprint (which was not certified by peer review) is the author/funder. All rights reserved. No reuse allowed without permission.

Table 2. Study Cohort. Pulmonary and Immune-Related Comorbidities in the Study.

	Donor	Death Post Infection (DPI)	Comorbidities	
			Pulmonary	**Others**
Aged RF-Bcl6no/low	**Donor 1**	4	COPD not staged. / Former smoker (58py), stopped 3 years ago.	Bipolar disorder, under lithium treatment. / Substituted hypothyroidism. / Systemic hypertension with peripheral arterial disease.
	Donor 2	8	h/o community acquired pneumonia 1 year ago. / h/o pulmonary embolism (right middle and inferior lobe) 1 year ago.	Severe scoliosis. / Femoral head prosthesis for 2 years. / History of TURP.
	Donor 3	1	Sleep apnea syndrome.	Follicular lymphoma grade I-II (in remission). / Lymphopenia (0.23G/L). / Hypothyroidism (substitution therapy). / Mixed anxiety-depressive disorder (treated with Citalopram). / Cardiomyopathy (arrhythmogenic, hypertensive, and toxic due to chemotherapy). / Systemic hypertension.
	Donor 4	19	-	Choledocholithiasis. / Cholecystectomy for cholecystolithiasis. / Minor neurocognitive disorders not investigated. / Myocardial amyloidosis
	Donor 5	4	History of heavy smoking (50 pack-years), currently abstinent.	Large-cell neuroendocrine carcinoma with unknown primary, diagnosed in January 2021, and a history of squamous cell carcinoma of the uvula and soft palate treated in 2012. / Inflammatory anemia related to neoplasia. / Proximal deep vein thrombosis (DVT) in the left lower extremity due to active cancer. / Peripheral artery disease in the lower limbs. / History of alcohol consumption (now abstinent). / Treated hypothyroidism. / Systemic hypertension.
	Donor 6	-	Pulmonary Langerhans cell histiocytosis (lung transplant in 2004, on immunosuppressants).	Cervico-dorsal myelopathy (inflammatory origin), severe cognitive impairment (related to COVID-19 encephalopathy and possible neurodegenerative disorder). / Treated hypertension and hypercholesterolemia. / Ulcers on both ankles, vertebral fracture at T10 with osteopenia. / Neurogenic bladder with urinary incontinence. / Multiple pancreatic cystic lesions (IPMNs), vulvar condylomas, and cervical dysplasia (treated with conization in 2014).
	Donor 7	-	-	Alcohol-related liver cirrhosis (CHILD B). / Atrial fibrillation. / Treated hypertension. / Monoclonal B-cell lymphocytosis without palpable lymphadenopathy. / Severe thrombocytopenia.
	Donor 8	15	COPD with asthma component. / Active smoking (80py).	Alcoholism. / Prostate cancer (autopsy finding). / DM type II. / Systemic hypertension with peripheral arterial disease.
	Donor 9	14	-	Squamous cell carcinoma of the lung (autopsy finding). / Paranoid schizophrenia (institutionalized patient). / History of breast carcinoma (8 years ago). / Malnutrition. / Systemic hypertension.
	Donor 10	-	-	-
	Donor 11	55	Obstructive Sleep Apnea Syndrome (SAOS), managed with CPAP.	Treated hypertension and hypercholesterolemia. / Moderate mitral insufficiency. / Cerebral aneurysm rupture in 1990 with placement of a ventricular drain. / Right brachio-crural motor hemiparesis of indeterminate origin. / Vascular encephalopathy.
	Donor 26	39	Chronic Obstructive Pulmonary Disease (COPD). / Bilateral lung transplant (3 years prior).	Heart failure. / Diabetes.
	Donor 27	17	-	Hypertension. / Diabetes.
Aged RF-Bcl6int	**Donor 12**	12	COPD stage II. / Asthma.	Prostate cancer (autopsy finding). / Pancreatic neuroendocrine tumor (autopsy finding). / Ankylosing spondylarthritis. / History of cerebellar ischemic stroke (9 years ago). / DM type II. / Dyslipidemia. / AVB 1st degree and LAFB.
	Donor 13	-	-	Dilated cardiomyopathy (mixed: ischemic, hypertensive, genetic). / History of coronary stenting. / Automatic defibrillator (for 9 years). / Systemic hypertension. / Dyslipidemia.
	Donor 14	38	-	High-grade papillary urothelial carcinoma (pT2b pN0 R0 M0) with Bricker urinary diversion. / Hypertensive heart disease. / Treated hypertension. / Type 2 diabetes (non-insulin-dependent, treated). / Overweight (BMI 29 kg/m²). / Treated dyslipidemia.
	Donor 15	1	-	Second-degree atrioventricular block (AV block). / Myocardial amyloidosis. / Severe coronary artery disease. / Treated hypertension. / Alzheimer's-type degenerative encephalopathy, Braak stage 3. / Cerebro-meningeal amyloid angiopathy. / Osteoporosis.

bioRxiv preprint doi: https://doi.org/10.1101/2024.11.07.622471; this version posted November 8, 2024. The copyright holder for this preprint (which was not certified by peer review) is the author/funder. All rights reserved. No reuse allowed without permission.

	Donor 16	-	-	Heart failure with preserved EF, managed with pacemaker and conservative treatment for coronary issues. / Treated hypertension. / History of prostate and joint surgeries (hip and shoulder). / Multifactorial balance issues, mild neurocognitive decline, and suspected lacunar stroke. / Anemia, mild Amiodarone-induced hyperthyroidism, and previous drug-induced skin reaction.
Aged RF-Bcl6high	**Donor 17**	4	-	DM type II. / Dyslipidemia.
	Donor 18	9	COPD stage III. / Asthma. / Sleep apnea syndrome.	Mixed anxiety-depressive disorder (treated). / Hiatal hernia. / Substituted hypothyroidism following subtotal thyroidectomy for multinodular goiter. / Arrhythmogenic cardiomyopathy (pacemaker). / Systemic hypertension.
	Donor 19	23	Former smoker.	**Metatarso-phalangeal osteoarthritis (left hallux) due to diabetic foot ulcer with** secondary bacteremia (methicillin-susceptible Staphylococcus aureus and Proteus mirabilis) (1 month before death). / DM type II. / Hypertrophic and valvular cardiomyopathy. / History of aortic valve replacement. / Pacemaker due to complete heart block. / Systemic hypertension.
	Donor 20	11	-	Treated hypertension (Exforge). / Liver steatosis, colonic polyps (2014, 2018), and gastroesophageal reflux (2001). / Suspected right ureteropelvic junction disorder and history of ureteral stone (1989). / Dupuytren's disease.
	Donor 21	16	Neuroendocrine small-cell lung carcinoma with bone and liver metastases, diagnosed in September 2019. Under palliative treatment. / Former smoker (50 pack-years), quit in 2016.	Left foot drop likely due to peripheral involvement. / Coronary artery disease with NSTEMI in December 2016 and stent placement in the marginal and right coronary arteries.
	Donor 22	13	-	Regenerative normocytic normochromic anemia. /Acute confusional state (hypo and hyperactive) of multifactorial origin. / Gait and balance instability. / Mixed anxiety-depressive disorder. / Moderate mental retardation. / History of hysterectomy (not dated). / Ischemic cardiomyopathy. / History of myocardial infarction (not dated). / History of myocarditis 8 years ago.
Young RF-Bcl6no/low	**Donor 23**	20		GE reflux. / Gout. / Seizure disorder. / Gunshot wound 1985 (head and chest). / Hypertension. / Stroke. / Hyperlipidemia.
	Donor 24-a / Donor 24-b	40	-	Obesity. / Diabetes. / Central Hypothyroidism. / Hypertension. / Hyperlipidemia.
	Donor 25	30	-	Alcoholic Cirrhosis. / Hepatic Encephalopathy. / Obesity. / Gastric Bypass surgery.
	Donor 28	50	Asthma.	Obesity. / Systemic Lupus Erythematosus. / Sickle cell trait.
Young RF-Bcl6int	**Donor 29-a / Donor 29-b**	47	-	Obesity.
	Donor 30	27	-	Hyperlipidemia.
Young RF-Bcl6high	**Donor 31**	14	-	Tetraplegia (due to a road accident 13 years ago).

bioRxiv preprint doi: https://doi.org/10.1101/2024.11.07.622471; this version posted November 8, 2024. The copyright holder for this preprint (which was not certified by peer review) is the author/funder. All rights reserved. No reuse allowed without permission.

Table 3. List of primary antibodies used in the study. The origin source (host), clone, isotype and vendor are provided.

Primary Antibodies	*Host*	*Clonality*	*Clone*	*Isotype*	*Vendor*	*Cat #*
PD1	mouse	monoclonal	NAT 105	IgG1κ	Biocare medical	ACI 3137
CD57	mouse	monoclonal	NK-1	IGMκ	Diagnostic BioSystem	Mob 163
Bcl-6	mouse	monoclonal	GI191E/A8	IgG	CELL MARQUE	760-4241
CD20	mouse	monoclonal	L26	IgG1κ	Novocastra-Leica	NCL-L-CD20-L26
CD4	rabbit	monoclonal	SP35	IgG	VENTANA MEDICAL	790-4423
Ki67	mouse	monoclonal	MIB-1	IgG1κ	DAKO	M7240
GrzB	mouse	monoclonal	GrB-7	IgG2a	MONOSAN	MON7029C
CD8	mouse	monoclonal	C8/144B	IgG1κ	DAKO	M7103
CD14	rabbit	monoclonal	EPR3653	IgG	CELL MARQUE	114R-15
MPO	rabbit	polyclonal	EPR4793	IgG	abcam	AB9535
CD68	mouse	monoclonal	PG-M1	IgG3κ	DAKO	M0876
FDC	mouse	monoclonal	CNA.42	IGM	Invitrogen	14-9968-82

Table 4. The multiplex panels applied are shown. The primary antibodies /opal fluorochromes and the application order of all primary antibodies used in a given panel are shown.

Panel	Order	Primary Antibody	Dilution	Opal Fluorophore	Dilution
Adaptive Immunity	1	**PD1**	1/100	opal 620	1/150
	2	**CD57**	1/300	opal 570	1/150
	3	**Bcl-6**	dispenser	opal 480	1/150
	4	**CD20**	1/400	opal 520	1/150
	5	**CD4**	1/200	opal 690	1/200
	6	**Ki67**	1/300	opal 780	1/25
Innate Immunity	1	**GzrB**	1/40	opal 570	1/150
	2	**CD8**	1/100	opal 690	1/150
	3	**CD20**	1/400	opal 480	1/700
	4	**CD14**	1/50	opal 620	1/150
	5	**MPO**	1/150	opal 520	1/150
	6	**CD68**	1/200	opal 780	1/25
FDC panel	1	**FDC**	1/200	alexa 488	1/150
	4	**CD20**	1/45	conj-ef650	1/150

Table 5. Donors used for the analysis of GC reactivity in Hilar vs. matched control Subdiaphragmatic LNs.

Donor	Origin	Gender	Age (Years)
Donor 3	Switzerland	M	72
Donor 9	Switzerland	F	73
Donor 11	Switzerland	F	76
Donor 15	Switzerland	M	86
Donor 14	Switzerland	M	74
Donor 17	Switzerland	M	87
Donor 21	Switzerland	M	65

bioRxiv preprint doi: https://doi.org/10.1101/2024.11.07.622471; this version posted November 8, 2024. The copyright holder for this preprint (which was not certified by peer review) is the author/funder. All rights reserved. No reuse allowed without permission.

Table 6. Summary of Statistical Analysis for Cell Population Comparisons: Raw and FDR-adjusted P-values with Significance Indicators Across Multiple Main Figures.

Figure	Cell Population	Comparison Group	Comparison	Raw p-value	Significance symbol Raw p-value	FDR-adjusted p-value	Significance symbol FDR-adjusted p-value
Figure 1C	CD20hi Ki67hibcl6hi	Aged	GC-Bcl6no/low vs GC-Bcl6high	0.0001	***	0.0006	***
			GC-Bcl6no/low vs GC-Bcl6int	0.0006	***	0.0018	***
			GC-Bcl6int vs GC-Bcl6high	0.0043	**	0.0086	**
		Young	GC-Bcl6no/low vs GC-Bcl6int	0.0536	ns	0.0804	ns
		Aged vs Young	Aged GC-Bcl6no/low vs Young GC-Bcl6no/low	0.9391	ns	0.9391	ns
			Aged GC-Bcl6int vs Young GC-Bcl6int	0.0714	ns	0.08568	ns
Figure 1D	Normalized Follicle Areas (µm2)	x	GC-Bcl6no/low vs GC-Bcl6high	<0.0001	****	0.00015	****
			GC-Bcl6no/low vs GC-Bcl6int	<0.0001	****	0.00015	****
			GC-Bcl6int vs GC-Bcl6high	0.115	ns	0.115	ns
Figure 1E	CD20hi - count per (µm2)	Aged	GC-Bcl6no/low vs GC-Bcl6high	0.8201	ns	0.8201	ns
			GC-Bcl6no/low vs GC-Bcl6int	0.6461	ns	0.8201	ns
			GC-Bcl6int vs GC-Bcl6high	0.7922	ns	0.8201	ns
		Young	GC-Bcl6no/low vs GC-Bcl6int	0.0357	*	0.2142	ns
		Aged vs Young	Aged GC-Bcl6no/low vs Young GC-Bcl6no/low	0.2343	ns	0.4686	ns
			Aged GC-Bcl6int vs Young GC-Bcl6int	0.0714	ns	0.2142	ns
	CD20hiKi67hi - count per (µm2)	Aged	GC-Bcl6no/low vs GC-Bcl6high	0.0047	**	0.0282	**
			GC-Bcl6no/low vs GC-Bcl6int	0.0194	*	0.0582	*
			GC-Bcl6int vs GC-Bcl6high	0.4286	ns	0.51432	ns
		Young	GC-Bcl6no/low vs GC-Bcl6int	0.1429	ns	0.2858	ns
		Aged vs Young	Aged GC-Bcl6no/low vs Young GC-Bcl6no/low	0.9593	ns	0.9593	ns
			Aged GC-Bcl6int vs Young GC-Bcl6int	0.25	ns	0.375	ns
	CD20hiKi67hiBcl6hi - count per (µm2)	Aged	GC-Bcl6no/low vs GC-Bcl6high	0.0001	***	0.0006	***
			GC-Bcl6no/low vs GC-Bcl6int	0.0023	**	0.0006	**
			GC-Bcl6int vs GC-Bcl6high	0.0519	ns	0.07785	ns
		Young	GC-Bcl6no/low vs GC-Bcl6int	0.1429	ns	0.17148	ns
		Aged vs Young	Aged GC-Bcl6no/low vs Young GC-Bcl6no/low	0.5575	ns	0.5575	ns
			Aged GC-Bcl6int vs Young GC-Bcl6int	0.0357	*	0.0714	ns
Figure 2D	PD1hi - count per (µm2)	Aged	GC-Bcl6no/low vs GC-Bcl6high	0.0002	***	0.0009	***
			GC-Bcl6no/low vs GC-Bcl6int	0.0003	***	0.0009	***
			GC-Bcl6int vs GC-Bcl6high	0.4286	ns	0.42886	ns
		Young	GC-Bcl6no/low vs GC-Bcl6int	0.0714	ns	0.1428	ns
		Aged vs Young	Aged GC-Bcl6no/low vs Young GC-Bcl6no/low	0.233	ns	0.3495	ns
			Aged GC-Bcl6int vs Young GC-Bcl6int	0.3929	ns	0.42886	ns
	PD1hiKi67hi - count per (µm2)	Aged	GC-Bcl6no/low vs GC-Bcl6high	0.0001	***	0.0006	***
			GC-Bcl6no/low vs GC-Bcl6int	0.0011	**	0.0033	**
			GC-Bcl6int vs GC-Bcl6high	0.9307	ns	0.9307	ns
		Young	GC-Bcl6no/low vs GC-Bcl6int	0.0357	*	0.0714	ns
		Aged vs Young	Aged GC-Bcl6no/low vs Young GC-Bcl6no/low	0.171	ns	0.2565	ns
			Aged GC-Bcl6int vs Young GC-Bcl6int	0.25	ns	0.3	ns
	PD1hiCD57hi - count per (µm2)	Aged	GC-Bcl6no/low vs GC-Bcl6high	0.0002	***	0.0012	***
			GC-Bcl6no/low vs GC-Bcl6int	0.0123	*	0.0369	*
			GC-Bcl6int vs GC-Bcl6high	0.9307	ns	0.9307	ns
		Young	GC-Bcl6no/low vs GC-Bcl6int	0.0714	ns	0.1428	ns
		Aged vs Young	Aged GC-Bcl6no/low vs Young GC-Bcl6no/low	0.1816	ns	0.2724	ns
			Aged GC-Bcl6int vs Young GC-Bcl6int	0.3929	ns	0.47148	ns
	PD1hiKi67hiBcl6hi - count per (µm2)	Aged	GC-Bcl6no/low vs GC-Bcl6high	0.0001	***	0.0006	***
			GC-Bcl6no/low vs GC-Bcl6int	0.042	*	0.0792	ns
			GC-Bcl6int vs GC-Bcl6high	0.7922	ns	0.7922	ns
		Young	GC-Bcl6no/low vs GC-Bcl6int	0.0179	*	0.0537	*
		Aged vs Young	Aged GC-Bcl6no/low vs Young GC-Bcl6no/low	0.0528	ns	0.0792	ns
			Aged GC-Bcl6int vs Young GC-Bcl6int	0.3929	ns	0.47148	ns
Figure 3D	Area aboce and below the curve (µm2) GC B cells CD20hiKi67hiBcl6hi	x	Tonsils vs GC-Bcl6int	0.0009	***	0.00135	***
			Tonsils vs GC-Bcl6high	0.0004	***	0.0012	***
			GC-Bcl6int vs GC-Bcl6high	0.8793	ns	0.8793	ns
	Area aboce and below the curve (µm2) TFH cells PD1hi CD57hi	x	Tonsils vs GC-Bcl6int	0.1475	ns	0.22125	ns
			Tonsils vs GC-Bcl6high	0.0042	**	0.0126	**
			GC-Bcl6int vs GC-Bcl6high	0.3434	ns	0.3434	ns
Figure 5C	CD8hi Total cell counts	Aged	GC-Bcl6no/low vs GC-Bcl6high	0.2129	ns	0.7404	ns
			GC-Bcl6no/low vs GC-Bcl6int	0.8788	ns	0.9999	ns
			GC-Bcl6int vs GC-Bcl6high	0.2468	ns	0.7404	ns
		Young	GC-Bcl6no/low vs GC-Bcl6int	>0.9999	ns	0.9999	ns
		Aged vs Young	Aged GC-Bcl6no/low vs Young GC-Bcl6no/low	0.7214	ns	0.9999	ns
			Aged GC-Bcl6int vs Young GC-Bcl6int	0.7857	ns	0.9999	ns
	CD8hi GrzBhi Total cell counts	Aged	GC-Bcl6no/low vs GC-Bcl6high	0.0831	ns	0.4287	ns
			GC-Bcl6no/low vs GC-Bcl6int	0.799	ns	0.799	ns
			GC-Bcl6int vs GC-Bcl6high	0.4286	ns	0.799	ns
		Young	GC-Bcl6no/low vs GC-Bcl6int	0.1429	ns	0.4287	ns
		Aged vs Young	Aged GC-Bcl6no/low vs Young GC-Bcl6no/low	0.5743	ns	0.799	ns
			Aged GC-Bcl6int vs Young GC-Bcl6int	0.7857	ns	0.799	ns
	MPOhi Total cell counts	Aged	GC-Bcl6no/low vs GC-Bcl6high	0.5532	ns	0.66384	ns
			GC-Bcl6no/low vs GC-Bcl6int	0.2786	ns	0.4179	ns
			GC-Bcl6int vs GC-Bcl6high	0.0173	*	0.1038	ns
		Young	GC-Bcl6no/low vs GC-Bcl6int	0.7857	ns	0.7857	ns
		Aged vs Young	Aged GC-Bcl6no/low vs Young GC-Bcl6no/low	0.1946	ns	0.3892	ns
			Aged GC-Bcl6int vs Young GC-Bcl6int	0.0357	*	0.1071	ns
	CD14hi Total cell counts	Aged	GC-Bcl6no/low vs GC-Bcl6high	0.1246	ns	0.2492	ns
			GC-Bcl6no/low vs GC-Bcl6int	0.799	ns	0.799	ns
			GC-Bcl6int vs GC-Bcl6high	0.4286	ns	0.51432	ns
		Young	GC-Bcl6no/low vs GC-Bcl6int	0.3929	ns	0.51432	ns
		Aged vs Young	Aged GC-Bcl6no/low vs Young GC-Bcl6no/low	0.0365	*	0.1095	ns
			Aged GC-Bcl6int vs Young GC-Bcl6int	0.0357	*	0.1095	ns
	CD68hi Total cell counts	Aged	GC-Bcl6no/low vs GC-Bcl6high	0.0529	ns	0.07935	ns
			GC-Bcl6no/low vs GC-Bcl6int	0.5058	ns	0.5058	ns
			GC-Bcl6int vs GC-Bcl6high	0.1775	ns	0.213	ns
		Young	GC-Bcl6no/low vs GC-Bcl6int	0.0357	*	0.0714	ns
		Aged vs Young	Aged GC-Bcl6no/low vs Young GC-Bcl6no/low	0.0268	*	0.0714	ns
			Aged GC-Bcl6int vs Young GC-Bcl6int	0.0357	*	0.0714	ns

bioRxiv preprint doi: https://doi.org/10.1101/2024.11.07.622471; this version posted November 8, 2024. The copyright holder for this preprint (which was not certified by peer review) is the author/funder. All rights reserved. No reuse allowed without permission.

Table 7. Summary of Statistical Analysis for Cell Population Comparisons: Raw and FDR-adjusted P-values with Significance Indicators Across Multiple Supplementary Figures.

Figure	Cell Population	Comparison Group	Comparison	Raw p-value	Significance symbol Raw p-value	FDR-adjusted p-value	Significance symbol FDR-adjusted p-value
Suppl. Figure 1B	CD20hi - Total cell counts	Aged	GC-Bcl6no/low vs GC-Bcl6high	0.0135	*	0.0405	*
			GC-Bcl6no/low vs GC-Bcl6int	0.5058	ns	0.60696	ns
			GC-Bcl6int vs GC-Bcl6high	0.0043	**	0.0258	**
		Young	GC-Bcl6no/low vs GC-Bcl6int	0.0357	*	0.05355	*
		Aged vs Young	Aged GC-Bcl6no/low vs Young GC-Bcl6no/low	0.799	ns	0.799	ns
			Aged GC-Bcl6int vs Young GC-Bcl6int	0.0357	*	0.05355	*
	CD20hiKi67hi - Total cell counts	Aged	GC-Bcl6no/low vs GC-Bcl6high	0.0001	***	0.0006	***
			GC-Bcl6no/low vs GC-Bcl6int	0.0037	**	0.0111	**
			GC-Bcl6int vs GC-Bcl6high	0.0303	*	0.0606	ns
		Young	GC-Bcl6no/low vs GC-Bcl6int	0.0714	ns	0.08568	ns
		Aged vs Young	Aged GC-Bcl6no/low vs Young GC-Bcl6no/low	0.4905	ns	0.4905	ns
			Aged GC-Bcl6int vs Young GC-Bcl6int	0.0714	ns	0.08568	ns
	CD20hiKi67hiBcl6hi - Total cell counts	Aged	GC-Bcl6no/low vs GC-Bcl6high	0.0001	***	0.003	***
			GC-Bcl6no/low vs GC-Bcl6int	0.0006	***	0.003	***
			GC-Bcl6int vs GC-Bcl6high	0.0043	**	0.0086	**
		Young	GC-Bcl6no/low vs GC-Bcl6int	0.0536	ns	0.0804	ns
		Aged vs Young	Aged GC-Bcl6no/low vs Young GC-Bcl6no/low	0.9391	ns	0.9391	ns
			Aged GC-Bcl6int vs Young GC-Bcl6int	0.0714	ns	0.08568	ns
	Frequency of CD20hi cells (% of total cells)	Aged	GC-Bcl6no/low vs GC-Bcl6high	0.6165	ns	0.7857	ns
			GC-Bcl6no/low vs GC-Bcl6int	0.4421	ns	0.7857	ns
			GC-Bcl6int vs GC-Bcl6high	0.6623	ns	0.7857	ns
		Young	GC-Bcl6no/low vs GC-Bcl6int	0.0357	*	0.1071	ns
		Aged vs Young	Aged GC-Bcl6no/low vs Young GC-Bcl6no/low	0.0061	**	0.0366	*
			Aged GC-Bcl6int vs Young GC-Bcl6int	0.7857	ns	0.7857	ns
	Frequency of CD20hiKi67hi cells (% of total cells)	Aged	GC-Bcl6no/low vs GC-Bcl6high	0.0002	***	0.0009	***
			GC-Bcl6no/low vs GC-Bcl6int	0.0003	***	0.0009	***
			GC-Bcl6int vs GC-Bcl6high	0.4286	ns	0.6429	ns
		Young	GC-Bcl6no/low vs GC-Bcl6int	>0.9999	ns	0.9999	ns
		Aged vs Young	Aged GC-Bcl6no/low vs Young GC-Bcl6no/low	0.7214	ns	0.86568	ns
			Aged GC-Bcl6int vs Young GC-Bcl6int	0.0357	*	0.0714	ns
	Frequency of CD20hiKi67hiBcl6hi cells (% of total cells)	Aged	GC-Bcl6no/low vs GC-Bcl6high	0.0001	***	0.0006	***
			GC-Bcl6no/low vs GC-Bcl6int	0.0011	**	0.0033	**
			GC-Bcl6int vs GC-Bcl6high	0.0173	*	0.0346	*
		Young	GC-Bcl6no/low vs GC-Bcl6int	0.6964	ns	0.83568	ns
		Aged vs Young	Aged GC-Bcl6no/low vs Young GC-Bcl6no/low	0.941	ns	0.941	ns
			Aged GC-Bcl6int vs Young GC-Bcl6int	0.0357	*	0.05355	*
Suppl. Figure 1D	PD1hi - Total cell counts	Aged	GC-Bcl6no/low vs GC-Bcl6high	0.0001	***	0.0006	***
			GC-Bcl6no/low vs GC-Bcl6int	0.0003	***	0.0009	***
			GC-Bcl6int vs GC-Bcl6high	>0.9999	ns	0.9999	ns
		Young	GC-Bcl6no/low vs GC-Bcl6int	0.0714	ns	0.1428	ns
		Aged vs Young	Aged GC-Bcl6no/low vs Young GC-Bcl6no/low	0.8521	ns	0.9999	ns
			Aged GC-Bcl6int vs Young GC-Bcl6int	>0.9999	ns	0.9999	ns
	PD1hiKi67hi - Total cell counts	Aged	GC-Bcl6no/low vs GC-Bcl6high	0.0001	***	0.0006	***
			GC-Bcl6no/low vs GC-Bcl6int	0.0011	**	0.0033	**
			GC-Bcl6int vs GC-Bcl6high	0.329	ns	0.3948	ns
		Young	GC-Bcl6no/low vs GC-Bcl6int	0.0357	*	0.0714	ns
		Aged vs Young	Aged GC-Bcl6no/low vs Young GC-Bcl6no/low	0.1299	ns	0.19485	ns
			Aged GC-Bcl6int vs Young GC-Bcl6int	0.5714	ns	0.5714	ns
	PD1hiCD57hi - Total cell counts	Aged	GC-Bcl6no/low vs GC-Bcl6high	0.0002	***	0.0012	***
			GC-Bcl6no/low vs GC-Bcl6int	0.0006	***	0.0018	***
			GC-Bcl6int vs GC-Bcl6high	0.2468	ns	0.3702	ns
		Young	GC-Bcl6no/low vs GC-Bcl6int	0.125	ns	0.25	ns
		Aged vs Young	Aged GC-Bcl6no/low vs Young GC-Bcl6no/low	0.3298	ns	0.39576	ns
			Aged GC-Bcl6int vs Young GC-Bcl6int	0.7857	ns	0.7857	ns
	PD1hiKi67hiBcl6hi - Total cell counts	Aged	GC-Bcl6no/low vs GC-Bcl6high	<0.0001	****	0.0006	****
			GC-Bcl6no/low vs GC-Bcl6int	0.0385	*	0.077	ns
			GC-Bcl6int vs GC-Bcl6high	0.2662	ns	0.3993	ns
		Young	GC-Bcl6no/low vs GC-Bcl6int	0.0357	*	0.077	ns
		Aged vs Young	Aged GC-Bcl6no/low vs Young GC-Bcl6no/low	0.4312	ns	0.51744	ns
			Aged GC-Bcl6int vs Young GC-Bcl6int	0.6429	ns	0.6429	ns
	Frequency of PD1hi cells (% of total cells)	Aged	GC-Bcl6no/low vs GC-Bcl6high	0.0003	***	0.0009	***
			GC-Bcl6no/low vs GC-Bcl6int	0.0003	***	0.0009	***
			GC-Bcl6int vs GC-Bcl6high	0.5368	ns	0.64416	ns
		Young	GC-Bcl6no/low vs GC-Bcl6int	0.0536	ns	0.1071	ns
		Aged vs Young	Aged GC-Bcl6no/low vs Young GC-Bcl6no/low	0.6947	ns	0.6947	ns
			Aged GC-Bcl6int vs Young GC-Bcl6int	0.0714	ns	0.1071	ns
	Frequency of PD1hiKi67hi cells (% of total cells)	Aged	GC-Bcl6no/low vs GC-Bcl6high	0.0004	***	0.0024	***
			GC-Bcl6no/low vs GC-Bcl6int	0.1228	ns	0.3684	ns
			GC-Bcl6int vs GC-Bcl6high	0.2468	ns	0.3702	ns
		Young	GC-Bcl6no/low vs GC-Bcl6int	0.2321	ns	0.3702	ns
		Aged vs Young	Aged GC-Bcl6no/low vs Young GC-Bcl6no/low	0.6214	ns	0.74568	ns
			Aged GC-Bcl6int vs Young GC-Bcl6int	0.7857	ns	0.7857	ns
	Frequency of PD1hiCD57hi cells (% of total cells)	Aged	GC-Bcl6no/low vs GC-Bcl6high	0.0071	**	0.0261	**
			GC-Bcl6no/low vs GC-Bcl6int	0.059	ns	0.118	ns
			GC-Bcl6int vs GC-Bcl6high	0.4286	ns	0.51432	ns
		Young	GC-Bcl6no/low vs GC-Bcl6int	0.1429	ns	0.21435	ns
		Aged vs Young	Aged GC-Bcl6no/low vs Young GC-Bcl6no/low	0.0087	**	0.0261	**
			Aged GC-Bcl6int vs Young GC-Bcl6int	0.5714	ns	0.5714	ns
	Frequency of PD1hiKi67hiBcl6hi cells (% of total cells)	Aged	GC-Bcl6no/low vs GC-Bcl6high	0.0001	***	0.0006	***
			GC-Bcl6no/low vs GC-Bcl6int	0.0701	ns	0.1402	ns
			GC-Bcl6int vs GC-Bcl6high	0.2468	ns	0.34668	ns
		Young	GC-Bcl6no/low vs GC-Bcl6int	0.0357	*	0.1071	ns
		Aged vs Young	Aged GC-Bcl6no/low vs Young GC-Bcl6no/low	0.2889	ns	0.34668	ns
			Aged GC-Bcl6int vs Young GC-Bcl6int	0.7857	ns	0.7857	ns

bioRxiv preprint doi: https://doi.org/10.1101/2024.11.07.622471; this version posted November 8, 2024. The copyright holder for this preprint (which was not certified by peer review) is the author/funder. All rights reserved. No reuse allowed without permission.

Acknowledgements

The authors would like to thank Dr Natalie Piazzon (operational director of the Tissue Biobank), Damien Maison and Emilie Lingre, Institute of Pathology, CHUV, for their help with the tissue processing.

Funding: these studies were supported by grants from the Swiss National Science Foundation (SNF, 310030_204226) to C.P. and by the Institute of Pathology, Department of Laboratory Medicine and Pathology, Lausanne University Hospital and Lausanne University, Lausanne, Switzerland. Any funding for the USA samples?

Authorship Contributions

C.B and K.I performed experiments and image analysis, S.G, and M.O contributed to image analysis, C.B and S.G drafted the manuscripts, M.B and R.G. performed and supervised the spatial transcriptomic analysis, C.B. participated in the transcriptomic analysis, S.B. and C.B. performed neighboring analysis, O.Y.C. supervised the statistical analysis, J.B supervised the SQL clustering analysis, M.S. and S.B. assisted with the clinical data, serological measurements and pathological evaluation/information, N.S. provided serological measurements, M.J.F, J.W.L. and L.de.L, provided tissue material and pathological information, G.P. assisted with the interpretation of the immunological data and the manuscript preparation, CP conceived, designed and supervised the study, interpreted data, and edited the manuscript. All authors have read, edited and approved the final version for submission.

Data sharing statement: The authors agree to share all publication-related data. For further information, please contact the corresponding author at Konstantinos.Petrovas@chuv.ch.

bioRxiv preprint doi: https://doi.org/10.1101/2024.11.07.622471; this version posted November 8, 2024. The copyright holder for this preprint (which was not certified by peer review) is the author/funder. All rights reserved. No reuse allowed without permission.

References

1. Kirtipal N, Bharadwaj S, and Kang SG. From SARS to SARS-CoV-2, insights on structure, pathogenicity and immunity aspects of pandemic human coronaviruses. *Infect Genet Evol.* 2020;85:104502.¨

2. Chen Y, Klein SL, Garibaldi BT, Li H, Wu C, Osevala NM, et al. Aging in COVID-19: Vulnerability, immunity and intervention. *Ageing Res Rev.* 2021;65:101205.

3. Connors J, Haddad EK, and Petrovas C. Aging alters immune responses to vaccines. *Aging (Albany NY).* 2021;13(2):1568-70.

4. Young C, and Brink R. The unique biology of germinal center B cells. *Immunity.* 2021;54(8):1652-64.

5. Mayberry CL, Logan NA, Wilson JJ, and Chang CH. Providing a Helping Hand: Metabolic Regulation of T Follicular Helper Cells and Their Association With Disease. *Front Immunol.* 2022;13:864949.

6. Kaneko N, Kuo HH, Boucau J, Farmer JR, Allard-Chamard H, Mahajan VS, et al. Loss of Bcl-6-Expressing T Follicular Helper Cells and Germinal Centers in COVID-19. *Cell.* 2020;183(1):143-57 e13.

7. Hu G, and Zhao K. Looping around Bcl6 in Germinal Center to Sharpen B Cell Immunity. *Immunity.* 2016;45(3):459-61.

8. Bibert S, Guex N, Lourenco J, Brahier T, Papadimitriou-Olivgeris M, Damonti L, et al. Transcriptomic Signature Differences Between SARS-CoV-2 and Influenza Virus Infected Patients. *Frontiers in Immunology.* 2021;12.

9. Ioannidou K, Ndiaye DR, Noto A, Fenwick C, Fortis SP, Pantaleo G, et al. In Situ Characterization of Follicular Helper CD4 T Cells Using Multiplexed Imaging. *Front Immunol.* 2020;11:607626.

10. Gerner MY, Kastenmuller W, Ifrim I, Kabat J, and Germain RN. Histo-cytometry: a method for highly multiplex quantitative tissue imaging analysis applied to dendritic cell subset microanatomy in lymph nodes. *Immunity.* 2012;37(2):364-76.

11. Virtanen P, Gommers R, Oliphant TE, Haberland M, Reddy T, Cournapeau D, et al. SciPy 1.0: fundamental algorithms for scientific computing in Python. *Nat Methods.* 2020;17(3):261-72.

12. Kang W. pysal/pointpats: pointpats 2.3.0. pysal/pointpats: pointpats 2.3.0.

13. Harris CR, Millman KJ, Van Der Walt SJ, Gommers R, Virtanen P, Cournapeau D, et al. Array programming with NumPy. *Nature.* 2020;585(7825):357-62.

14. Reeves J, DP ON GM, Yang Z, Zimmerman S, and Vitancol R. GeoMxWorkflows: GeoMx digital spatial profiler (DSP) data analysis workflows. *R package version.* 2023;1(0).

15. Ortogero N, Yang Z, Vitancol R, Griswold M, and Henderson D. GeomxTools: NanoString GeoMx Tools. *R package version.* 2022;1(0).

16. NanoStringNCTools AP. NanoString nCounter Tools. *R package version.* 2023;1(1).

bioRxiv preprint doi: https://doi.org/10.1101/2024.11.07.622471; this version posted November 8, 2024. The copyright holder for this preprint (which was not certified by peer review) is the author/funder. All rights reserved. No reuse allowed without permission.

17. Liu N, Bhuva DD, Mohamed A, Bokelund M, Kulasinghe A, Tan CW, et al. standR: spatial transcriptomic analysis for GeoMx DSP data. *Nucleic Acids Research.* 2024;52(1):e2-e.

18. Gagnon-Bartsch JA, Jacob L, and Speed TP. Removing unwanted variation from high dimensional data with negative controls. *Berkeley: Tech Reports from Dep Stat Univ California.* 2013:1-112.

19. Ritchie ME, Phipson B, Wu D, Hu Y, Law CW, Shi W, et al. limma powers differential expression analyses for RNA-sequencing and microarray studies. *Nucleic acids research.* 2015;43(7):e47-e.

20. Love MI, Huber W, and Anders S. Moderated estimation of fold change and dispersion for RNA-seq data with DESeq2. *Genome biology.* 2014;15:1-21.

21. Subramanian A, Tamayo P, Mootha VK, Mukherjee S, Ebert BL, Gillette MA, et al. Gene set enrichment analysis: a knowledge-based approach for interpreting genome-wide expression profiles. *Proceedings of the National Academy of Sciences.* 2005;102(43):15545-50.

22. Bhuva D, Smyth G, and Garnham A. Msigdb: an ExperimentHub package for the molecular signatures database (MSigDB). *R package version.* 2023;1(0).

23. Bhuva D. vissE: visualising set enrichment analysis results. *R package version.* 2021;122.

24. Bodelet J, and Shan J. Nonparametric additive factor models. *arXiv preprint arXiv:200313119.* 2020.

25. Padhan K, Moysi E, Noto A, Chassiakos A, Ghneim K, Perra MM, et al. Acquisition of optimal TFH cell function is defined by specific molecular, positional, and TCR dynamic signatures. *Proc Natl Acad Sci U S A.* 2021;118(18).

26. Alshekaili J, Chand R, Lee CE, Corley S, Kwong K, Papa I, et al. STAT3 regulates cytotoxicity of human CD57+ CD4+ T cells in blood and lymphoid follicles. *Sci Rep.* 2018;8(1):3529.

27. Pereira JP, Kelly LM, and Cyster JG. Finding the right niche: B-cell migration in the early phases of T-dependent antibody responses. *International immunology.* 2010;22(6):413-9.

28. Petrovas C, Ferrando-Martinez S, Gerner MY, Casazza JP, Pegu A, Deleage C, et al. Follicular CD8 T cells accumulate in HIV infection and can kill infected cells in vitro via bispecific antibodies. *Sci Transl Med.* 2017;9(373).

29. Brachtel EF, Washiyama M, Johnson GD, Tenner-Racz K, Racz P, and MacLennan IC. Differences in the germinal centres of palatine tonsils and lymph nodes. *Scand J Immunol.* 1996;43(3):239-47.

30. Kim CH, Rott LS, Clark-Lewis I, Campbell DJ, Wu L, and Butcher EC. Subspecialization of CXCR5+ T cells: B helper activity is focused in a germinal center-localized subset of CXCR5+ T cells. *J Exp Med.* 2001;193(12):1373-81.

31. Muus C, Luecken MD, Eraslan G, Sikkema L, Waghray A, Heimberg G, et al. Single-cell meta-analysis of SARS-CoV-2 entry genes across tissues and demographics. *Nat Med.* 2021;27(3):546-59.

bioRxiv preprint doi: https://doi.org/10.1101/2024.11.07.622471; this version posted November 8, 2024. The copyright holder for this preprint (which was not certified by peer review) is the author/funder. All rights reserved. No reuse allowed without permission.

32. Mothes R, Pascual-Reguant A, Koehler R, Liebeskind J, Liebheit A, Bauherr S, et al. Distinct tissue niches direct lung immunopathology via CCL18 and CCL21 in severe COVID-19. *Nat Commun.* 2023;14(1):791.

33. Huang I, and Pranata R. Lymphopenia in severe coronavirus disease-2019 (COVID-19): systematic review and meta-analysis. *J Intensive Care.* 2020;8:36.

34. Lee JY, Skon CN, Lee YJ, Oh S, Taylor JJ, Malhotra D, et al. The transcription factor KLF2 restrains CD4(+) T follicular helper cell differentiation. *Immunity.* 2015;42(2):252-64.

35. Taghavie-Moghadam PL, Waseem TC, Hattler J, Glenn LM, Dobrian AD, Kaplan MH, et al. STAT4 Regulates the CD8(+) Regulatory T Cell/T Follicular Helper Cell Axis and Promotes Atherogenesis in Insulin-Resistant Ldlr(-/-) Mice. *J Immunol.* 2017;199(10):3453-65.

36. Ma X, and Nakayamada S. Multi-Source Pathways of T Follicular Helper Cell Differentiation. *Front Immunol.* 2021;12:621105.

37. Weinstein JS, Laidlaw BJ, Lu Y, Wang JK, Schulz VP, Li N, et al. STAT4 and T-bet control follicular helper T cell development in viral infections. *J Exp Med.* 2018;215(1):337-55.

38. Dahlen E, Dawe K, Ohlsson L, and Hedlund G. Dendritic cells and macrophages are the first and major producers of TNF-alpha in pancreatic islets in the nonobese diabetic mouse. *J Immunol.* 1998;160(7):3585-93.

39. Shankwitz K, Pallikkuth S, Sirupangi T, Kirk Kvistad D, Russel KB, Pahwa R, et al. Compromised steady-state germinal center activity with age in nonhuman primates. *Aging Cell.* 2020;19(2):e13087.

40. Quig A, Kriachkov V, and King H. Mapping and modelling human B cell maturation in the germinal centre. *Curr Opin Immunol.* 2024;87:102428.